School of Earth Sciences

A UK M_W catalogue derived from coda envelopes

Charlie Peach

A dissertation submitted to the University of Bristol in accordance with therequirements for award of the degree of Masters by Research in the schoolof Earth Sciences, in the Faculty of Science.

April 2024

Supervisors: Professor James Wookey and Dr Maximilian Werner

Word Count: 13,352

Abstract

The United Kingdom (UK) experiences low-to-moderate levels of seismicity; only 12 onshore earthquakes with local magnitude (ML) ≥ 4.0 have been recorded in the past 20 years. It is therefore difficult to estimate moment magnitude (M_W) using conventional moment tensor inversion for the majority of UK seismicity, resulting in limited reliable estimates of M_W. To address this, we calibrated coda envelopes at 16 broadband seismic stations distributed across the UK, to produce a M_W catalogue for 100 events with $M_W \geq 2.23$ that occurred since 2006. This was achieved using the open-source Coda Calibration Tool, which requires independent source parameter estimates for calibration. For 13 UK events between 2006 and 2022, we used spectral modelling to estimate apparent stress (0.55 to 4.13 MPa), and moment tensor inversion to estimate M_W (3.35 to 4.52). These independent source parameters formed a subset of the inputs into the final calibration, which used seismic data from 33 events with coda-derived values of $2.65 \leq Mw \leq 4.48$. The resultant coda calibration parameters were applied to 67 further events ($M_W \geq 2.23$). The coda envelopes exhibit slow seismic coda decay across the UK, with significant energy up to 20 Hz, consistent with other regions of low tectonic activity, such as Eastern Canada. This M_W catalogue, and the application of the calibration to future UK seismic events, will be useful for both assessing seismic hazard and event characterisation.

Acknowledgments

I would like to express my deepest gratitude and appreciation to all the individuals and organisations who have contributed to the completion of this research. Without their support, guidance, and encouragement, this work would not have been possible.

First and foremost, I am immensely grateful to my supervisors - both from the Atomic Weapons Establishment (AWE) and the University of Bristol (UoB). From AWE, I would like to thank Dr. Stuart Nippress and Dr. David Green, and from UoB, I would like to thank Professor James Wookey and Dr Maximilian Werner. Their guidance and expertise has been invaluable, as well as their feedback and improvements made to this manuscript. Additionally, I would like to thank Dr. Robert Myhill and Professor Ben Edwards for their feedback and the subsequent modifications made to this manuscript. Furthermore, I would like to acknowledge the financial support provided by AWE and the BGS for providing the data required for this research.

Data Availability

Seismic data used in this study are available from ORFEUS (https://www.orfeus-eu.org) and IRIS (http://ds.iris.edu/ds/nodes/dmc/). MTtime (v1.1.0) was used for moment tensor inversion (https://github.com/LLNL/mttime). SpecMod (v0.1.1) was used for spectral modelling (https://github.com/uofuseismo/SpecMod). The Coda Calibration Tool (v1.0.18.3) was used to calibrate the UK and create the M_W catalogue (https://github.com/LLNL/coda-calibration-tool). Event information for international earthquakes (Table 4) are from the Saint Louis University Moment Tensor Determinations (last accessed 23/08/2022) (https://www.eas.slu.edu/eqc/eqcmt.html) and the Northern California Earthquake Data Center Catalog (last accessed 23/08/2022) (https://www.ncedc.org). Event information for UK earthquakes (Tables 1 to 3) comes from the BGS seismic bulletins (last accessed 23/08/2022) (https://www.earthquakes.bgs.ac.uk/publications/bulletins/bulletins_list.htm).

Author’s declaration

I declare that the work in this dissertation was carried out in accordance with the requirements of the University's Regulations and Code of Practice for Research Degree Programmes and that it has not been submitted for any other academic award. Except where indicated by specific reference in the text, the work is the candidate's own work. Work done in collaboration with, or with the assistance of, others, is indicated as such. Any views expressed in the dissertation are those of the author.

SIGNED: .....Charlie Peach..... DATE: ....08/04/2024.....

Students must sign the examination copies but should only print their name in the final version that they electronically submit so that no personal signifiers are shown in the online release of the dissertation.

TABLE OF CONTENTS

List of Figures

List of Tables

CHAPTER 1: Introduction

Measuring earthquake magnitudes in an area of relatively low seismic activity, such as the UK, can be a difficult process. This is because conventional methods of earthquake magnitude estimation are often unreliable when applied to low magnitude events. To address this, in this thesis we develop and test a workflow which can measure low magnitude seismic events via analysis of seismic coda.

1.1 Motivation

There are numerous magnitude scales for measuring seismic event size. Richter (1935) developed the first magnitude scale that measures the maximum-recorded signal amplitude, without distinguishing between seismic phases, for observations at seismic stations within 600 km of the earthquake. This magnitude scale, commonly referred to as the local magnitude (M_L), was developed for observations of earthquakes in Southern California (on a specific instrument – the Wood-Anderson seismograph) but continues to be used in local and regional seismic catalogues globally. The M_L formulation underestimates earthquake magnitudes for distant (> 600 km) earthquakes (where S-wave attenuation is not fully captured), deep earthquakes (where surface waves are smaller) and for large earthquakes (it does not take into account the duration of the shaking). Moment magnitude (M_W), derived from seismic moment (a measure of the energy released by the event, denoted M_0), is regarded as the most physically meaningful magnitude scale, since it does not saturate at large magnitudes (Hanks and Kanamori, 1979), and it can be directly related to, for example, geometric properties of the earthquake fault (e.g., Aki, 1966).

Robust estimation of M_W is vital in seismic monitoring for multiple reasons. Firstly, it is needed for creating accurate seismic catalogues, which are used in seismic hazard studies to highlight areas of high seismicity. Additionally, M_W estimates are used for characterising seismic sources. For example, event characterisation is required to discriminate between earthquakes and underground explosions, and M_W values can be used to estimate explosion yields (e.g., Pasyanos and Chiang, 2022). Accurate estimates of M_W are also important in seismic monitoring of subsurface resource operations, including mining, hydraulic fracturing, and geothermal energy. Finally, attempts at linking narrowband magnitudes (measured within

a narrow frequency range) such as M_L to M_w are often associated with significant bias (Shelly *et al.*, 2022) so an M_w methodology that can be applied for both small and large events is preferable.

1.2 Estimating seismic source parameters

Earthquake Moment Magnitude (M_W) is a vital seismic source parameter. M_W quantifies the size or magnitude of an earthquake, representing the total energy released during a seismic event, and can be written as:

$$M_W = \frac{2}{3}\log_{10}(M_0) - 6.03, \quad [1]$$

where M_0 is the seismic moment of the earthquake (Hanks and Kanamori, 1979). M_0 is determined from the earthquake's fault rupture area (A), slip distance along the fault plane (D), and rigidity of the Earth's crust (μ):

$$M_0 = \mu \times D \times A \quad [2]$$

An alternative method to measure the size of an earthquake is Local Magnitude (M_L), which is based on the amplitude of the recorded seismic waves. M_L can be written as:

$$M_L = \log_{10}(A) - \Delta, \quad [3]$$

where A is the maximum seismic wave amplitude recorded on a seismogram, and Δ is a correction for the effect of distance (Richter, 1935).

M_L and M_W each present distinct advantages and drawbacks. M_L offers a straightforward calculation process and easy interpretation, enabling quick assessments and benefiting from a wealth of historical data for long-term trend analysis and comparative studies. Nevertheless, its use diminishes for larger earthquakes due to saturation effects, and it heavily relies on the distance between the earthquake epicenter and the recording station, introducing variability in magnitude estimates across different regions. Conversely, M_W offers consistency in measurement across various magnitudes and geological settings, providing a more

comprehensive understanding of earthquake energy release through its consideration of seismic waves across a broader frequency band. Moreover, M_W proves less susceptible to saturation for exceptionally strong earthquakes, ensuring accurate assessments even for extreme events. However, the computation of M_W involves greater complexity and requires additional data inputs, posing challenges for real-time monitoring and rapid decision-making. Moreover, its shorter historical record compared to M_L limits its use for long-term trend analysis and retrospective studies.

Conventionally, estimates of seismic source parameters are calculated from long-period moment tensor inversions derived from waveform fitting using 1-D velocity models (e.g., Petersen *et al.*, 2021). Accurately estimating M_W from moment tensor inversions is dependent upon knowledge of the subsurface seismic velocity model. Inaccuracies in the velocity model result in inaccurate synthetic Green's functions, which are used to compute earthquake amplitudes by convolving them with the earthquake source time function, enabling the calculation of seismic waveforms at receiver locations. Therefore, inaccurate Green's functions (resulting from inaccurate seismic velocity models) can mis-predict amplitudes and therefore produce an unreliable M_W estimate. This is a disadvantage of the waveform modelling approach since the subsurface velocity structure is frequently poorly known and likely to vary, meaning 3-D seismic velocity models are required for different areas and source-station pairs. For smaller magnitude events ($M_W < 3.5$), this approach is also hampered by low signal-to-noise ratios (SNR) in the 10 - 20 second period band. Estimating earthquake magnitude via moment tensor inversion requires modelling of low frequency signal. For the low magnitude events commonly occurring in the UK, the SNR at low frequency can be less than or close to one. This prevents a reliable moment tensor inversion since the velocity models used for inversion are too low-resolution. As magnitude increases, there are lower frequencies for which the SNR > 1, meaning a low-resolution velocity model can yield a reliable moment tensor solution (see Figure 1 below for a schematic representation of this).

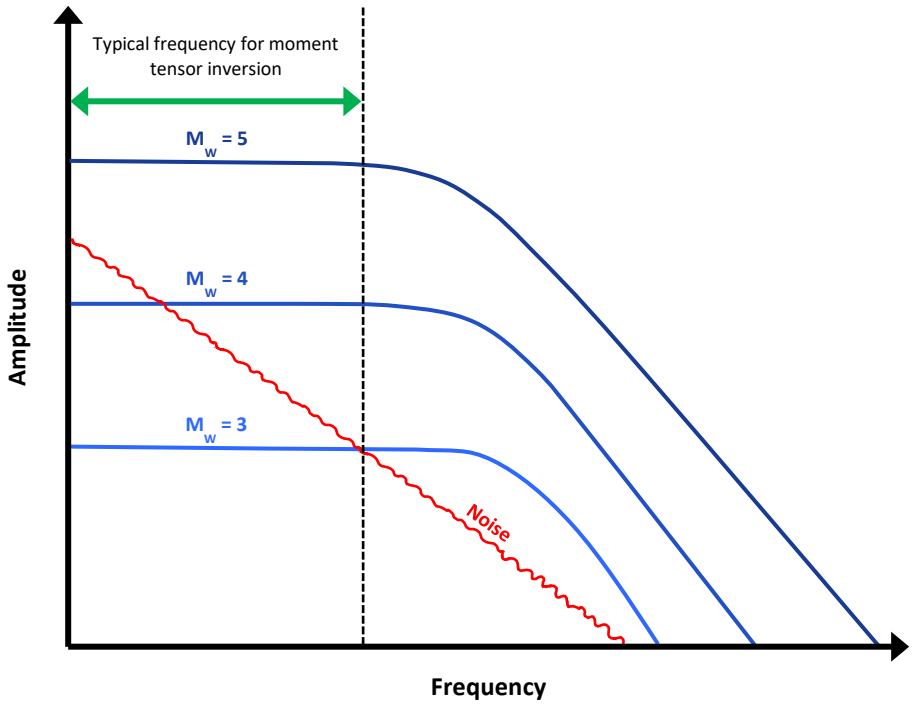

Figure 1 Schematic representation of approximate amplitude spectra for different magnitude events. This figure describes the difficulty in obtaining M_W estimates for low magnitude events via moment tensor inversion. For lower magnitude events (M_W = 3, light blue), the signal amplitude is above the noise level (red) for higher frequencies only compared to larger magnitude events (dark blue).

In the UK, there are limited reliable M_W estimates for seismic events below M_W = 3.5. A lack of an accurate knowledge of the UK 2-D and 3-D crustal structure, required for intermediate and short period waveform modelling, and the large computational expense in deriving complex Green's functions at shorter periods makes this technique difficult. This is important since M_W estimates can vary between studies, meaning it is hard to compare event M_W estimates if they are obtained via different techniques and with differing velocity models. One reason for this variability in M_W estimates is the complex structure and heterogeneity of the lithosphere (Gök *et al.*, 2019), which causes variation in the propagation of seismic waves. As a result, the recorded wave amplitude is likely different at each station. Due to lower SNRs, this wave amplitude variability has the largest influence on lower magnitude events, meaning identifying methods to estimate magnitudes for such events remains an active area of research (e.g., Laurendeau *et al.*, 2022).

Modelling high frequency seismic amplitude spectra is another approach for calculating source parameters (e.g., Holt *et al.*, 2021), such as apparent stress and M_W. These estimates can be influenced by heterogeneous path and site variations, and require significant

corrections that often require large amounts of data for path and site calibration (e.g., Oth *et al.*, 2011). As a result, creating a homogenous set of M_W estimates using either long-period moment tensors or modelling seismic amplitude spectra in the UK may be difficult for large catalogues that include events as small as M_W 2.5.

An alternative approach to calculating several earthquake source parameters, including Mw and apparent stress are seismic coda approaches (e.g., Mayeda and Walter, 1996). Seismic coda waves are a type of seismic signal that occurs after the initial arrival of primary and secondary seismic waves. These waves are a form of ground motion that persists even after the direct arrivals of the main seismic waves have passed. The coda waves arise from the complex interactions of seismic energy within the Earth's subsurface, including scattering, reflection, and diffraction (Figure 2).

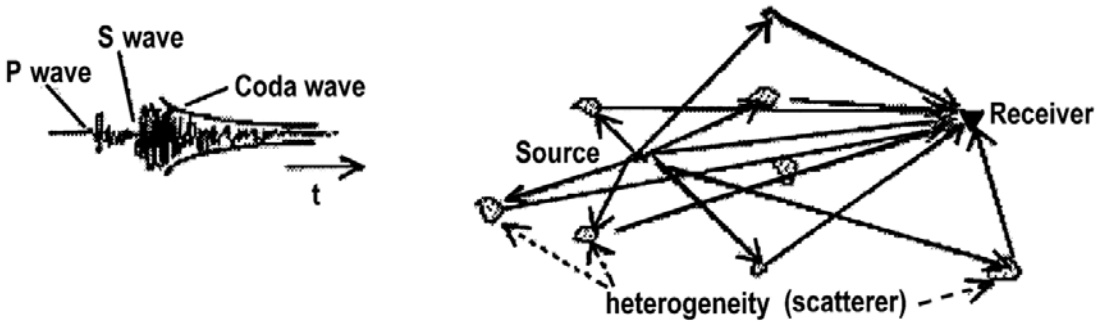

Figure 2 Schematic illustration of coda waves. Figure 3 from El-Hadidy et al. (2006).

As seismic waves travel through the Earth, they encounter various geological structures, interfaces, and heterogeneities. These interactions cause the seismic energy to scatter in multiple directions, resulting in a complex and less coherent pattern of ground motion at the station. The seismic coda is typically characterised by its long duration and decay in amplitude over time. The spatial averaging nature of the waves which make up the seismic coda mean that their spectral properties have significantly reduced sensitivity to 3D path heterogeneities at the low frequencies required to constrain M_W (Mayeda and Malagnini, 2010). Coda envelopes are also less affected by the radiation pattern and source directivity than direct waves (Aki and Chouet, 1975; Mayeda and Malagnini, 2010). As a result, source spectra, and hence seismic moment estimates from coda modelling, can be much more stable and robust than those derived from traditional direct wave approaches – up to four times less variable than those derived from conventional direct wave approaches (Morasca *et al.*, 2022;

Mayeda *et al.*, 2020). Coda methods are also applied across a wide passband, such that low magnitude events that are rich in high frequencies can also be analysed using this method. This is in contrast to the moment tensor inversion approach, where we are limited to the low-frequency component of the signal which is often much lower in SNR compared to the higher frequencies utilised in coda analyses.

1.3 Tectonic setting

The UK lies on the northwest part of the Eurasian tectonic plate, with the nearest plate boundary (the Mid-Atlantic ridge) over 1,500 km away. This tectonic setting is characterised by the interaction between the Eurasian Plate and the North American Plate, primarily along the North Atlantic region. The North Sea Basin, a result of Mesozoic rifting, remains an active area of tectonic activity. These ongoing tectonic interactions can lead to localised significant seismicity, as evidenced by historical events such as the 2008 Market Rasen earthquake (Ottemöller and Sargeant, 2010). The continental crust was formed in either the Precambrian or lower Palaeozoic age (Bluck *et al.*, 1992) by the amalgamation of several fault bounded terranes. Tectonic processes in the Caledonian (460 Ma) and Variscan (290 Ma) orogenies produced the current terrane configuration (Figure 3; Woodcock and Strachan, 2012).

As a result of its location, the UK is usually characterized as having low-moderate levels of seismicity (Musson, 2007), with ML^{BGS} (local magnitude calculated by the British Geological Survey, BGS) values seldom exceeding 5.0 (Figure 4). Observations dating back several hundred years suggest that people regularly feel earthquakes in the UK, but they rarely cause significant damage. Only 12 onshore earthquakes with $ML^{BGS} > 4.0$ have been recorded in the past 20 years and Musson (2007) estimates a 100-year return period for a ML^{BGS} 5.5 event.

The spatial distribution of seismicity varies significantly across the UK (Figure 4). The majority is found on the western flank of the UK in NW Scotland, across northern England, and in Wales, while eastern Scotland and southeast England are relatively aseismic. These earthquakes are generally considered to be due to the reactivation of existing faults by present-day deformation. However, surface ruptures are rarely reported for any UK

earthquakes (modern or historical) making it difficult to associate earthquakes with specific faults.

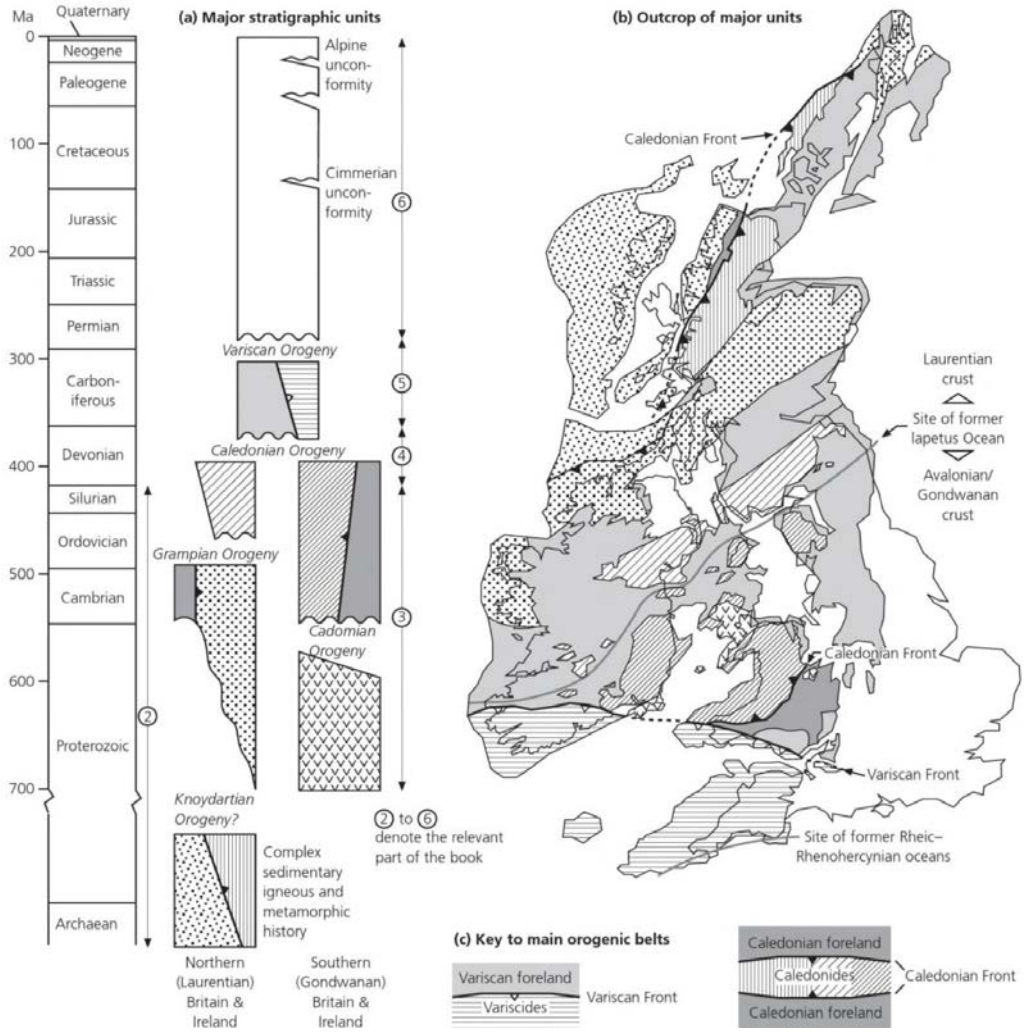

Figure 3 Figure 1.9 from Woodcock and Strachan (2012). Major tectonostratigraphic units in Britain and Ireland (a) with their outcrop distribution (b) and a key to the main orogenic belts (c).

The crustal strain field and its relation to the observed distribution of UK seismicity is unclear, with suggestions that it is related to glacio-isostatic rebound (e.g., Main *et al.*, 1999), as well as upwelling of hot material from the original Iceland plume head, causing uplift of the crust and driving tensional loading stresses (e.g., Arrowsmith *et al.*, 2005). Resolving these outstanding questions would be significantly helped with more robust and extensive catalogues of reliable earthquake magnitudes.

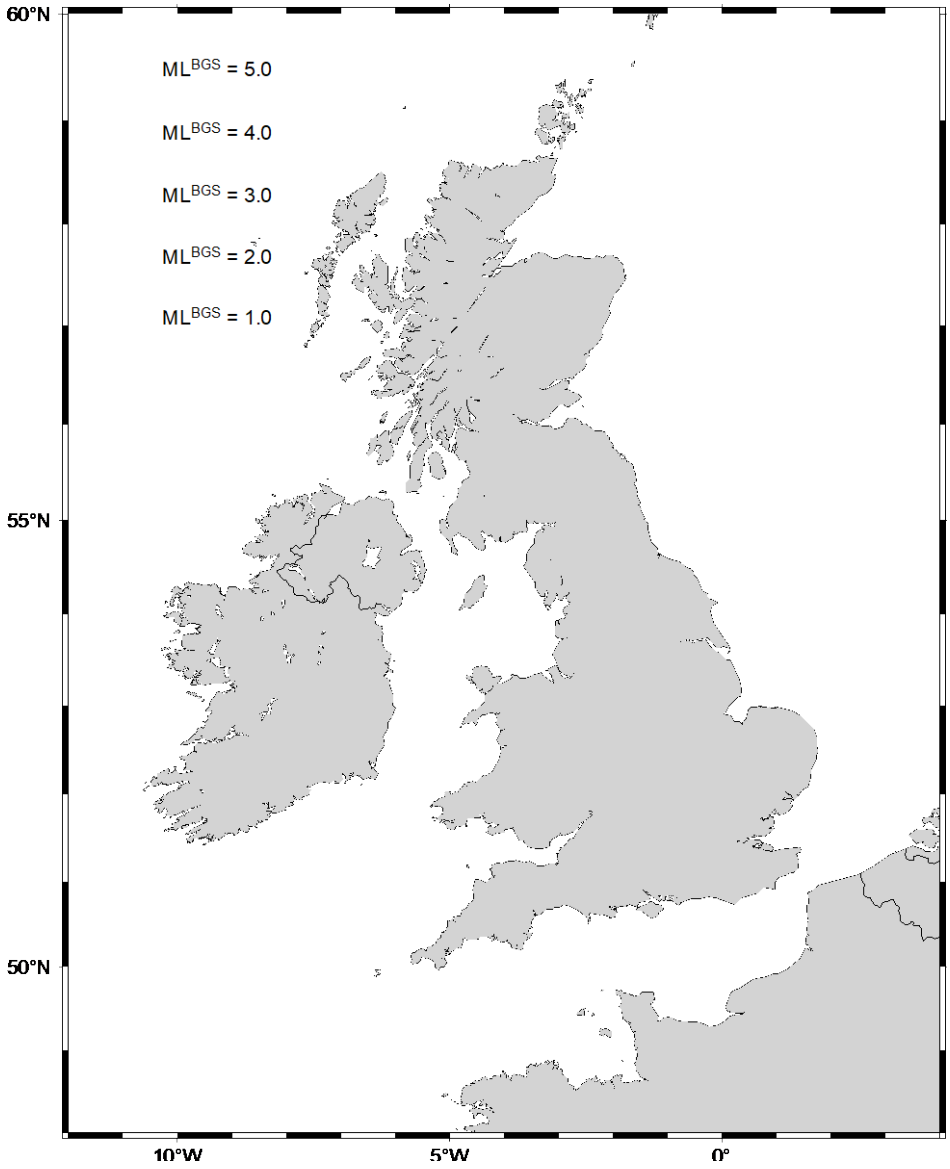

Figure 4 Regional seismicity in Britain and Ireland since 2006, where event symbol sizes are scaled by the event ML^{BGS} estimate. Event locations are from the BGS earthquake bulletin (e.g., Galloway, 2021).

1.4 Current UK Earthquake cataloguing

The BGS operates a nationwide network of seismograph stations in the UK and produces an annual bulletin of earthquakes located in the UK mainland and coastal waters. The BGS bulletin contains locations, local magnitudes (ML^{BGS}) and phase data but does not include estimates of M_W, primarily due to the difficulty in obtaining stable M_W estimates via waveform modelling in an area of low magnitude and low-to-moderate seismicity levels. M_W estimates for UK earthquakes are currently only available on an ad hoc basis as part of individual studies (e.g., Edwards *et al.*, 2008; Sargeant and Ottemöller, 2009; Ottemöller and

Sargeant, 2010) for a limited number of events. Thus, there is an opportunity to explore other approaches to creating more extensive, consistent M_W catalogues for the UK.

1.5 Aims and Objectives

The aim of this study is to create and test and workflow to generate a new M_W catalogue from coda wave envelopes. As discussed, this approach has advantageous features compared to other methods, potentially allowing estimations of M_W at magnitudes not feasible using traditional techniques (e.g., direct waveform modelling). Seismic coda analysis for M_W has been undertaken in various tectonic settings, including high heat flow regions such as the western US (e.g., Mayeda and Walter, 1996), cratonic regions like eastern Canada (e.g., Woodgold, 1990), the complex faulting region of central and northern Italy (Morasca *et al.*, 2008; Morasca *et al.*, 2022), the Arabian Peninsula (e.g., Chiang *et al.*, 2021), and western India (e.g., Malagnini *et al.*, 2006). Our study thus enables comparisons to be made between UK seismic coda envelopes and those in different tectonic regimes with distinctly different seismic attenuation (Q), heat flow, and tectonic history.

1.6 Collaboration and contributions

The work in this thesis forms the basis of a journal article submitted to Geophysical Journal Internation (Ref: GJI-S-23-0346). The work in the thesis was carried out by me, in collaboration with my supervisors – Dr. Stuart Nippress and Dr. David Green from the Atomic Weapons Establishment (AWE), and Professor James Wookey and Dr Maximilian Werner from the University of Bristol (UoB). Section 4.3 benefitted from discussions with Kevin Mayeda, who is far more experienced in using CCT in different tectonic regimes.

CHAPTER 2: Estimating seismic source parameters

In order to apply a seismic coda method to the UK seismic dataset (described below), we need to develop a workflow to properly calibrate and validate the approach. To do this we require independent estimates of Mw for comparison. We do this using two different methods. The first uses waveform modelling and moment tensor inversion to obtain estimates

of moment magnitude, M_W. The second method focuses on modelling seismic spectra to provide estimates of both apparent stress and M_W. These three methods are described below.

2.1 Dataset

We use three-component broadband (100 Hz sampling rate) data from seismic stations in the UK, Ireland and continental Europe (Figure 5). The majority of the data we use are from the BGS seismic network and from UKNET sites run by the Atomic Weapons Establishment (AWE) Blacknest, which are available to download from Observatories and Research Facilities for European Seismology (ORFEUS). Data from stations in Ireland (Irish National Seismic Network), France (CEA/DASE Seismic Network), Germany (German Regional Seismic Network), Luxembourg (Luxembourg Seismic Network), and the Netherlands (Netherlands Seismic and Acoustic Network) were also used and data were downloaded from the Incorporated Research Institutions for Seismology (IRIS).

Signals from low-moderate magnitude events ($M_W < 4.0$), such as those in the UK, are rarely observed at distances beyond 800 km. The moment tensor inversions and spectral modelling used data from stations within 800 km of the source. Using seismic stations at this distance range also ensured we had sufficient azimuthal coverage for reliable moment tensor solutions. For coda calibration, data from only UK stations were used (13 BGS and three UK-Net stations were used, Figure 4b), to avoid source-station paths with significantly different crustal properties. These UK stations were selected based on their longevity, reliability, and spatial distribution within the UK. In total 100 events across 62 stations were used (Figure 5).

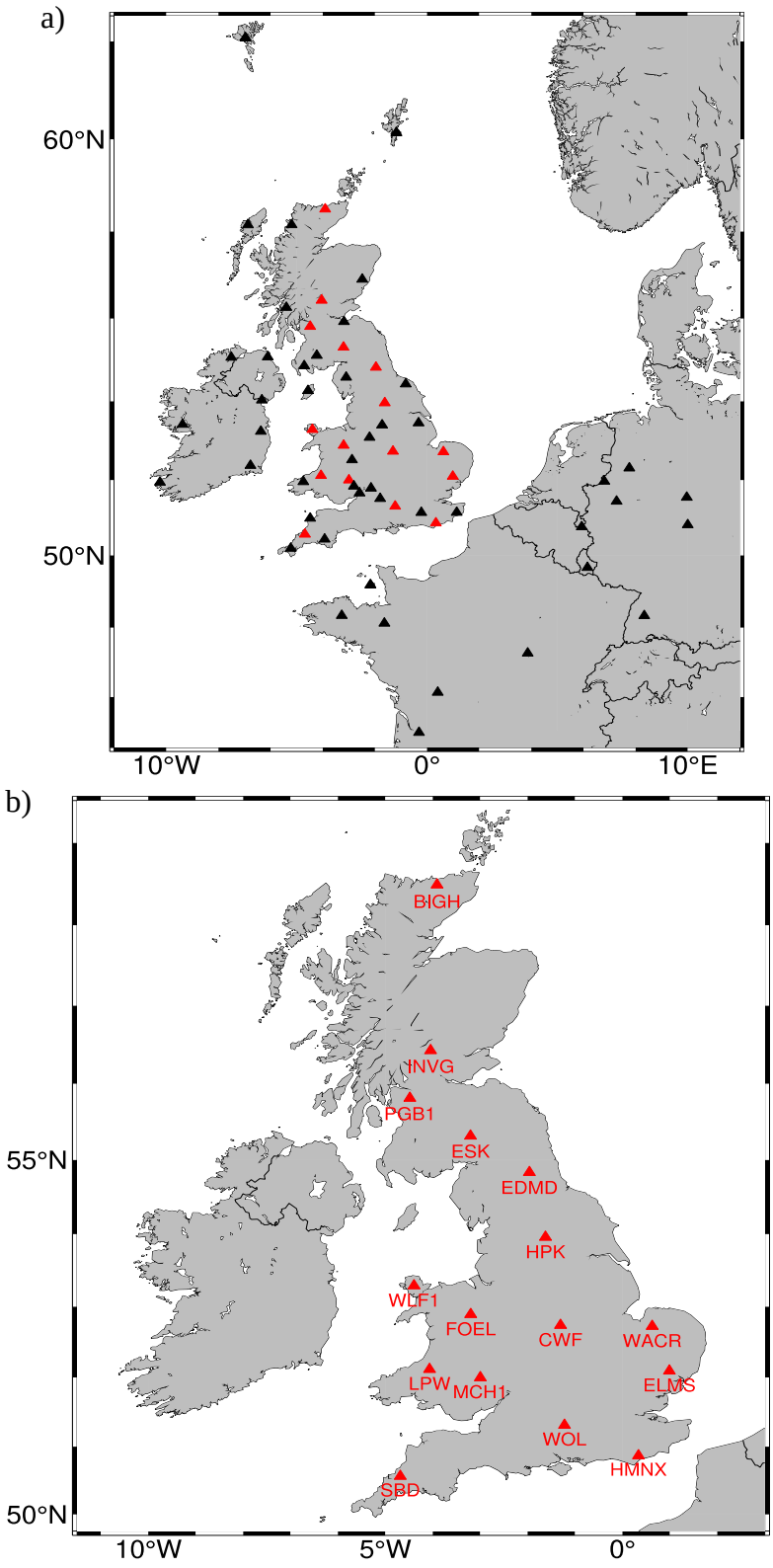

Figure 5 a) Distribution of stations (triangles) used throughout our study for independent source parameter estimates. (b) Stations used for coda calibration only. Stations coloured red represent those used for coda calibration, with labels for reference, whereas black stations were used only for independent source parameter estimates (via moment tensor inversion and spectral modelling).

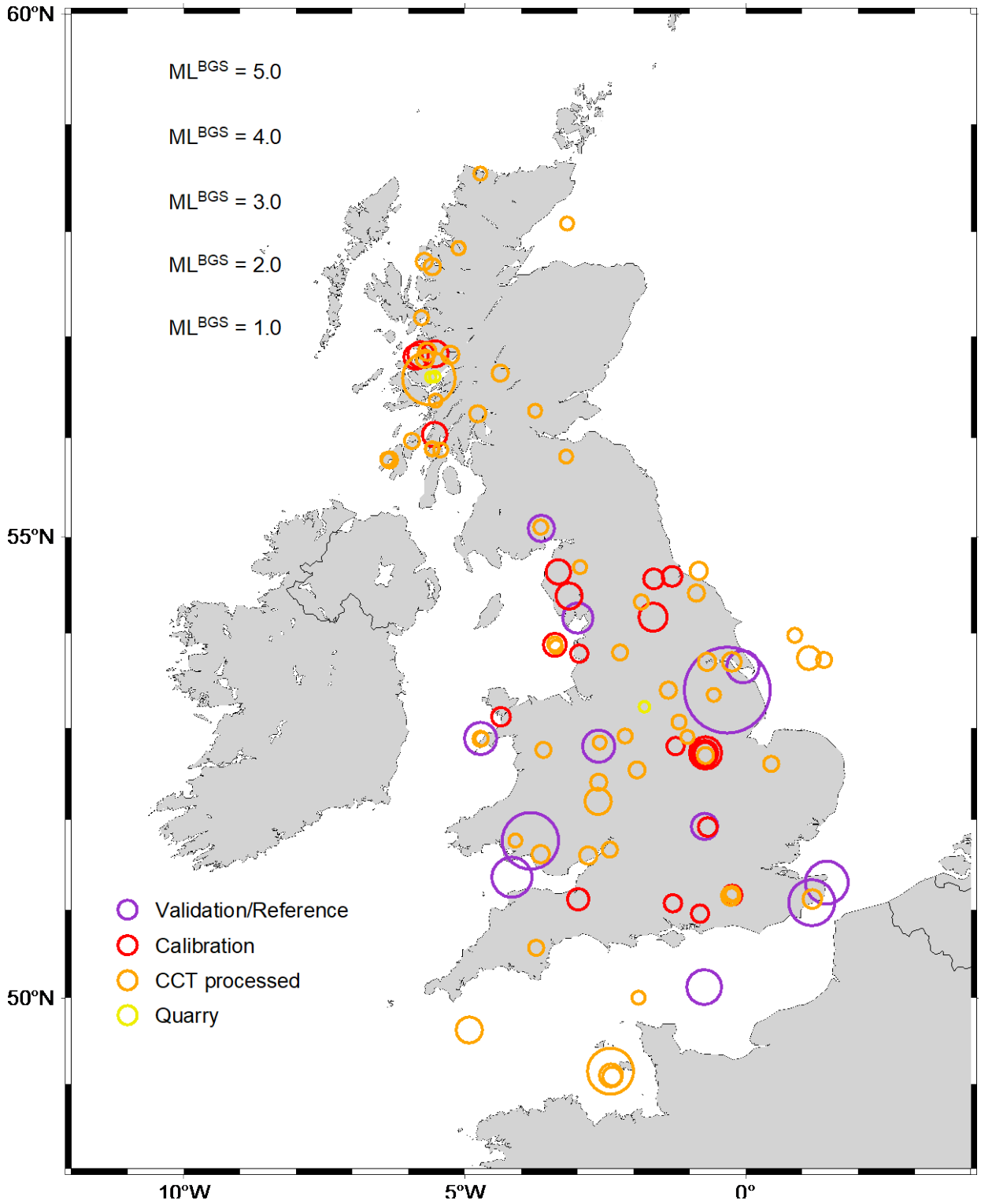

Figure 6 Events processed in this study (coloured circles), overlying regional seismicity since 2006 (grey circles). This event dataset includes both validation and reference events with independent source parameter estimates (purple), additional calibration events (red), natural events processed using CCT (orange), and CCT-processed quarry events (yellow). symbol sizes are scaled by the event ML^{BGS} estimate. Event locations are from the BGS earthquake bulletin (e.g., Galloway, 2021).

2.2 Methodology

We use the empirical method outlined by Mayeda *et al.* (2003), and described below, which offers an efficient method for calibrating and processing envelopes of seismic coda (Barno, 2017).

The coda calibration process requires independent reference earthquake source estimates (M_W and apparent stress) as constraints to determine each station's frequency-dependent site term correction. We refer to these events as *reference events*. *Validation events* – for which we also have independent M_W estimates – are used to evaluate the performance of the coda calibration. Additionally, *calibration* events are later included in the coda calibration process. These events do not have independent source estimates previously calculated but are used to help constrain the path terms associated with the calibration. Once this process is completed the calibrated tool can then be applied to further (past and future) events without modification to determine their moment magnitudes.

Only limited M_W estimates for UK seismicity are reported and are generally only available as part of individual studies (e.g., Sargeant and Ottemöller, 2009; Ottemöller and Sargeant, 2010) of a limited number of events. The methods used to infer M_W also differ between studies, and thus the estimated M_W can vary for the same event. Therefore, we instead make our own independent estimates of M_W by moment tensor inversion (Section 2.2.1) to ensure consistency. For each station's high frequency site term correction, independent estimates of apparent stress are used in the coda calibration and are preferable to assuming, *a priori*, a source scaling for the region (e.g., Morasca *et al.*, 2022). Apparent stress estimates for UK seismicity are limited. Therefore, spectral modelling (Section 2.2.2) was used to estimate independent apparent stress and M_W for the coda calibration process.

The complete workflow is shown in Figure 7.

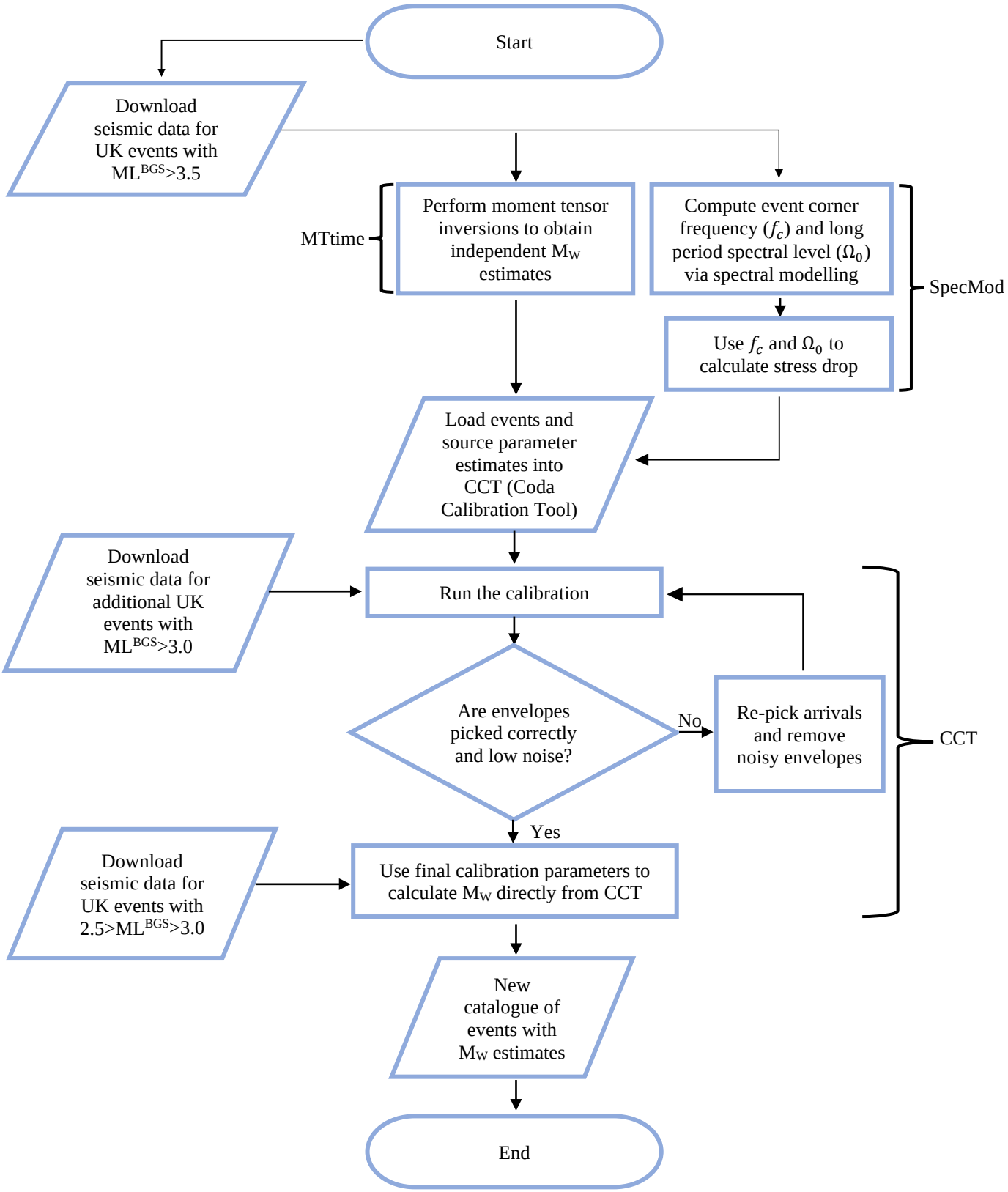

Figure 7 Workflow used for this study.

2.2.1 Moment tensor inversion to determine M_W

Our M_W estimates were calculated using MTtime, a Python package for time-domain moment tensor inversion (Chiang and USDOE, 2020) that estimates the deviatoric focal mechanism using the approach outlined by Minson and Dreger (2008). We follow the same procedure as described in previous studies (e.g., Chiang *et al.*, 2016; Chiang *et al.*, 2021). Observed waveform data are instrument corrected to displacement and then bandpass filtered (with the highpass corner between 0.02 - 0.05 Hz and the lowpass corner between 0.06 - 0.13 Hz, depending on the frequency content observed for each event). A Hanning taper is then applied to smooth and simplify the waveforms.

Green's functions (GFs) are calculated for each source-receiver pair in the same frequency range as the observed data, using the frequency-wavenumber integration method (Wang and Hermann, 1980) in Computer Programs in Seismology (Herrmann, 2013). The best-fitting moment tensor solution is computed by inverting the time-domain waveform data using a least squares minimisation approach (Minson and Dreger, 2008). This technique measures the fit between the observed and synthetic data over the length of the trace by the variance reduction (VR):

$$\mathrm{VR} = \left(1 - \frac{\sum_n w_n(\mathbf{d_n} - \mathbf{s_n})^2}{\sum_n w_n \mathbf{d_n}^2}\right) \times 100, \qquad [4]$$

where **d** is the data, **s** is the synthetic waveforms, and w is the inverse distance weighting factor at each station, n (Chiang *et al.*, 2016).

This method estimates the source depth by performing the inversion for a range of depths, with the preferred solution being that with the largest VR. The generation of GFs requires a velocity model. For this study, we use the ak135 velocity model (Kennett *et al.*, 1995), however we tested a range of alternative regional and global velocity models, including various BGS velocity models (e.g., Lownet and general UK, Mid Wales, Borders; Galloway, 2021), Preliminary Reference Earth Model (PREM; Dziewonski and Anderson, 1981), and a Western US model (Herrmann *et al.*, 2011). Though each velocity model largely retrieved consistent M_W estimates, the ak135 velocity model produced the largest VR for the 13 events

for which we calculated moment tensors. To account for uncertainties in the hypocenter parameters and the velocity model, small time shifts between the observed and synthetic seismograms are allowed (Pasyanos and Chiang, 2022). These time shifts are limited to half the minimum filtered period to avoid cycle skipping.

2.2.2 Spectral modelling to determine apparent stress and M_W

We also use SpecMod, a Python-based toolbox for processing and modelling seismic spectra (Edwards *et al.*, 2010), to provide independent estimates of apparent stress (as well as stress drop) and M_W (allowing comparisons with estimated M_W values from the moment tensor inversion described above).

Stress drop refers to the reduction in stress across a fault during an earthquake as the fault slips and releases stored elastic energy. Stress drop is a fundamental parameter used to characterise the strength of an earthquake source and is related to the seismic moment released during the earthquake. On the other hand, apparent stress is a measure of the average stress acting on the fault during the earthquake rupture, calculated based on seismic observations. It represents the stress that would be required to produce the observed level of ground shaking or seismic energy release. Apparent stress provides insights into the dynamic properties of earthquake sources and the frictional behavior of faults during slip. It is often estimated using empirical relationships between seismic moment, earthquake source parameters, and observed ground motion characteristics.

We follow a similar procedure to other studies (e.g., Holt *et al.*, 2021). The horizontal components of the observed waveforms are instrument corrected to velocity and rotated to radial and transverse components. Signal and noise windows are extracted from the transverse component, which is the preferred component for isolating the S-wave signal. The signal window starts at 95% of the elapsed time between the P and S arrivals and ends 20 – 30 s later. The noise window ends 2 s before the P arrival and is of equal length to the signal window. The signal and noise spectra are computed using the multi-taper approach (Prieto *et al.*, 2009). Finally, for each velocity spectrum we only fit the model between frequencies where the spectral SNR is greater than 3. If the spectral SNR is greater than 3 across the entire observed signal spectra, the lower frequency limit is set at 0.2 Hz (where the low-

frequency surface wave appears to dominate) and the upper frequency limit is set at 40 Hz. The velocity spectra, $A(f)$ are modelled using the Brune (1970) model:

$$\log_{10} A(f) = \log_{10} 2\pi f + \log_{10} \Omega_0 - \log_{10} \left[1 + \left(\frac{f}{f_c}\right)^2\right] - \frac{\pi f t^*}{\ln 10}, \quad [5]$$

where f is frequency (Hz), Ω_0 is the long-period spectral level at the source (m/s), f_c is corner frequency (Hz), and t^* is an attenuation parameter.

The Brune model provides a framework for explaining the mechanisms underlying earthquake generation and the subsequent release of seismic energy. This model conceptualises earthquakes as sudden ruptures along fault planes, resulting in the instantaneous release of stored elastic strain energy. Central to the Brune model is the representation of seismic moment release over time through a simple source time function, often approximated by a symmetric, impulsive pulse. Additionally, the model incorporates considerations of the radiation pattern of seismic waves and relates M_0 to observable parameters such as earthquake magnitude and f_c of the seismic spectrum.

We constrain Ω_0, f_c, and t^* using Powell's minimisation technique (Powell, 1964). Following Holt *et al.* (2021), we perform this inversion in two stages. First, we let all parameters be free and compute the best fitting Ω_0, f_c, and t^* at each station. We then calculate the average weighted f_c for the event, where each station's weight equates to the inverse of the hypocentral distance to the event. Second, we repeat the inversion with f_c fixed to this average value. Performing the inversion in this way helps resolve the trade-off between f_c and t^* (Holt *et al.*, 2021).

Before calculating M_0 from Ω_0, we use f_c to calculate the rupture radius, r (assuming a circular fault; Madariaga, 1976):

$$r = \frac{kV_s}{f_c}, \quad [6]$$

where k is a constant related to the radiation pattern and V_s is the shear-wave velocity (m/s). For our study, we use $k = 0.21$ (Madariaga, 1976) and $V_s = 3460$ ms^{-1} (velocity in ak135 to a

depth of 20 km, the maximum source depth in our study). We then use r with Ω_0 to calculate M_0:

$$M_0 = \frac{4\pi\Omega_0 V_S^3 \rho r}{F\theta G(R)}, \quad [7]$$

where ρ is density (kg m^{-3}), F is the free surface amplification factor, $G(R)$ describes the geometric spreading as a function of hypocentral distance (R), and θ is an empirically derived parameter related to the S-wave radiation pattern, averaged over the full focal sphere. We use $\rho = 2800$ kg m^{-3}, $F = 2$, and $\theta = 0.55$ (Boore and Boatwright, 1984). Note, we assume that site amplification is negligible. The site corrections in this area fluctuate between low values of amplification and deamplification (Edwards et al., 2008), meaning the resultant averaged source estimates are minimally affected by this assumption. For the geometric spreading correction, we follow Herrmann and Kijko (1983):

$$G(R) = \begin{cases} R^{-1}, & R < 100 \text{ km} \\ (100 \times R)^{-\frac{1}{2}}, & R \geq 100 \text{ km} \end{cases}, \quad [8]$$

The geometric spreading correction has previously been used by Ottemöller and Sargeant (2010) for UK seismicity. This enables us to calculate M_W using equation 1 (Hanks and Kanamori, 1979).

Stress drop, σ, is calculated using:

$$\sigma = \frac{7M_0}{16r^3}. \quad [9]$$

Allowing us to empirically calculate apparent stress, τ_a:

$$\tau_a = \frac{\sigma}{4.3} \quad [10]$$

(Singh and Ordaz, 1994). For each event, this methodology results in estimates of M_W and apparent stress at every station. Finally, the mean network M_W and apparent stress for each event are determined.

2.2.3 Coda calibration methodology to determine Mw

Once we have estimates of M_W and apparent stress for our reference events, to estimate M_W for the whole dataset we use the Coda Calibration Tool (CCT; Barno, 2017) and follow the method described in Mayeda *et al.* (2003), which has been widely used in other studies (e.g., Chiang *et al.*, 2021; Morasca *et al.*, 2022; Shelly *et al.*, 2022).

The main principle behind the coda calibration method is rooted in empirical observation and data analysis, whereby multiple seismic instruments are calibrated by analysing coda waves from the same event. By studying the behavior of these later-arriving coda waves, the calibration fine-tunes the sensitivity and accuracy of seismometers, taking into account local geological conditions, instrumental variations, and other factors that can affect the recorded seismic data. Specifically, seismic coda duration, amplitude decay, and frequency content can be used to help estimate earthquake source parameters, such as moment magnitude, M_W. For example, comparing events in a similar location, longer coda durations and slower amplitude decay can be indicative of a larger magnitude event.

To constrain these coda properties using CCT, horizontal component velocity seismograms are initially filtered into 15 narrow passbands between 0.05 and 19 Hz. For each frequency band, f_b, the two bandpass filtered horizontal components are stacked to produce a single envelope (e.g., Figure 11a). A model envelope, $E(f_b, x, t)$, is then fit to the data using the appropriate propagation distance, x (km), and propagation time, t (s), using:

$$E(f_b, x, t) = W(f_b) \times S(f_b) \times T(f_b) \times P(f_b, x) \times H\left(t - \frac{r}{v(f_b, x)}\right) \times \left(t - \frac{r}{v(f_b, x)}\right)^{-\gamma(f,r)} \exp\left[\beta(f_b, x) \times \left(t - \frac{r}{v(f_b, x)}\right)\right], \quad [11]$$

where W is the S-wave source amplitude, S is the frequency-dependent site effect, T is the S-to-coda transfer function, P is the path correction, H is the Heaviside step function, v is the

propagation velocity (km/s) corresponding to the coda envelope peak amplitude, and γ and β are parameters associated with the coda shape (e.g., Mayeda *et al.*, 2003; Shelly *et al.*, 2022; Morasca *et al.*, 2022). The coda is fit across a specified time length, between the coda envelope peak amplitude and an end limit. The end limit is located immediately before the coda amplitude returns to the pre-arrival noise amplitude, provided there are no aftershocks (i.e., '*f-markers*' in Figure 11a). For UK earthquakes, we typically fit between 200 to 400 s of coda.

We perform CCT calibration iteratively (see Figure 7). This iterative approach allows quality control of the *f-marker* positions and exclusion of envelopes with significant noise, therefore the calibration parameters become increasingly robust. Initially this calibration procedure uses just the *reference* and *validation* events (Figure 6 and Table 3) before including progressively more *calibration* events with each iteration. These *calibration* events (Figure 6 and Table 3), which are vital when constraining path terms, were geographically well distributed around the UK, and specifically chosen to improve raypath coverage and therefore well-calibrated path terms.

Once source, site, transfer function, and path effects are corrected for, the envelope amplitudes are still dimensionless. Following Mayeda *et al.* (2003), the non-dimensional amplitudes are converted to seismic moment, M_0, using previously determined *reference events*. These events have independently estimated M_W and apparent stress values from our moment tensor inversions and spectral modelling, and are used to constrain the frequency-dependent site terms (e.g., Shelly *et al.*, 2022; Morasca *et al.*, 2022). We use the *validation events*, which also have independent estimates of M_W, to validate the reliability of the calibration.

The peak envelope amplitudes, representing M_0, across all passbands are combined to give a resultant source spectrum, which is fit using a Brune (1970) source model to determine M_W and apparent stress (Figure 11b). The derived calibration parameters can then be used to directly measure M_W and apparent stress for different events within the calibrated region and potentially for future events in routine processing.

CHAPTER 3:Results

3.1.1 Moment tensor solutions

We were able (using MTime) to calculate stable deviatoric moment tensor solutions for 13 UK events that are distributed across the region of interest (Figure 8, red circles), exhibit a range of magnitudes (ML^{BGS} between 3.5 and 5.2), and have high quality data leading to high values of VR. The resulting moment tensor solutions have M_W values between 3.35 and 4.52 (see Table 1 for full moment tensor inversion solutions).

An example deviatoric moment tensor solution from an earthquake in Cwmllynfell, South Wales (event J in Table 1) is shown in Figure 10. This solution demonstrates a good fit between the observed and synthetic waveforms, and the VR for this preferred solution is 89%. In addition, this example shows the lack of sensitivity to source depth, where VR appears almost constant between 10 - 20 km. This feature of the inversion arises since we are predominantly fitting long-period surface waves. Nevertheless, our estimated depth is consistent with that estimated by the BGS (to within ~5 km). Furthermore, the approach of computing solutions for a range of depths provides insight as to how the inferred double couple (DC) component of the focal mechanism changes with source depth (Figure 9b). For event J, the DC component is small at the shallowest and deepest depths, and large (86%) at the depth of the preferred solution.

Table 1 Moment tensor inversion results for earthquakes in our study. Event origin time, latitude, and longitude are from the BGS earthquake bulletin (e.g., Galloway, 2021).

Event ID	Origin time (Year-Month-Day	Lat (°)	Lon (°)	MT depth (km)	DC/CLVD (%)	ML_S^{BGS}	M_W	Mrr	Mtt	Mff	Mrt	Mrf	Mtf	Exponent (dyne-cm)	Locality
A	2006-12-26 10:40:04	55.09	-3.64	6	91/9	3.5	3.41	-2.12	9.64	-7.52	-1.87	-3.71	-9.94	20	Dumfries
B	2007-04-28 07:18:11	51.08	1.17	2	85/15	4.3	4.03	-5.52	8.60	-3.08	3.56	-6.44	-4.16	21	Folkestone
C	2008-02-27 00:56:47	53.40	-0.33	20	93/7	5.2	4.52	3.18	-3.36	0.18	2.86	-1.72	-4.22	22	Market Rasen
D	2009-04-28 10:22:09	54.16	-2.99	6	82/18	3.7	3.50	-1.67	-15.06	16.73	0.14	-1.02	-8.55	20	Morecambe
E	2011-07-14 06:59:10	50.12	-0.74	6	96/4	3.9	3.65	5.13	-0.92	-4.21	6.32	-12.62	-28.38	20	English Channel
F	2013-05-29 03:16:28	52.88	-4.72	11	99/1	3.8	3.59	-5.95	18.93	-12.98	-4.15	-10.38	-16.88	20	Lleyn Peninsula
G	2014-02-20 13:21:30	51.36	-4.16	8	81/19	4.1	3.63	3.37	12.03	-15.40	2.43	-7.61	-23.15	20	Bristol Channel
H	2015-05-22 01:52:17	51.30	1.44	13	86/14	4.2	3.67	1.95	-1.02	-0.93	-1.44	-2.10	-1.28	21	Ramsgate
I	2017-08-04 14:43:38	56.80	-5.89	9	99/1	4.0	3.67	0.03	-28.88	28.84	-3.09	-0.84	17.55	20	Moidart
J	2018-02-17 14:31:07	51.77	-3.83	15	86/14	4.6	4.03	-8.49	-81.18	89.67	0.50	-3.67	-75.75	20	Cwmllynfell
K	2018-06-09 22:14:28	53.65	-0.06	10	97/3	3.8	3.35	3.47	-11.09	7.62	0.86	-5.32	-2.07	20	Grimsby
L	2020-09-08 08:45:28	51.93	-0.74	3	86/14	3.5	3.47	-1.12	-5.17	6.29	-1.35	0.22	-14.56	20	Leighton Buzzard
M	2022-05-30 14:36:58	52.80	-2.62	9	88/12	3.8	3.45	-0.88	-6.31	7.19	0.25	2.25	-13.58	20	Wem

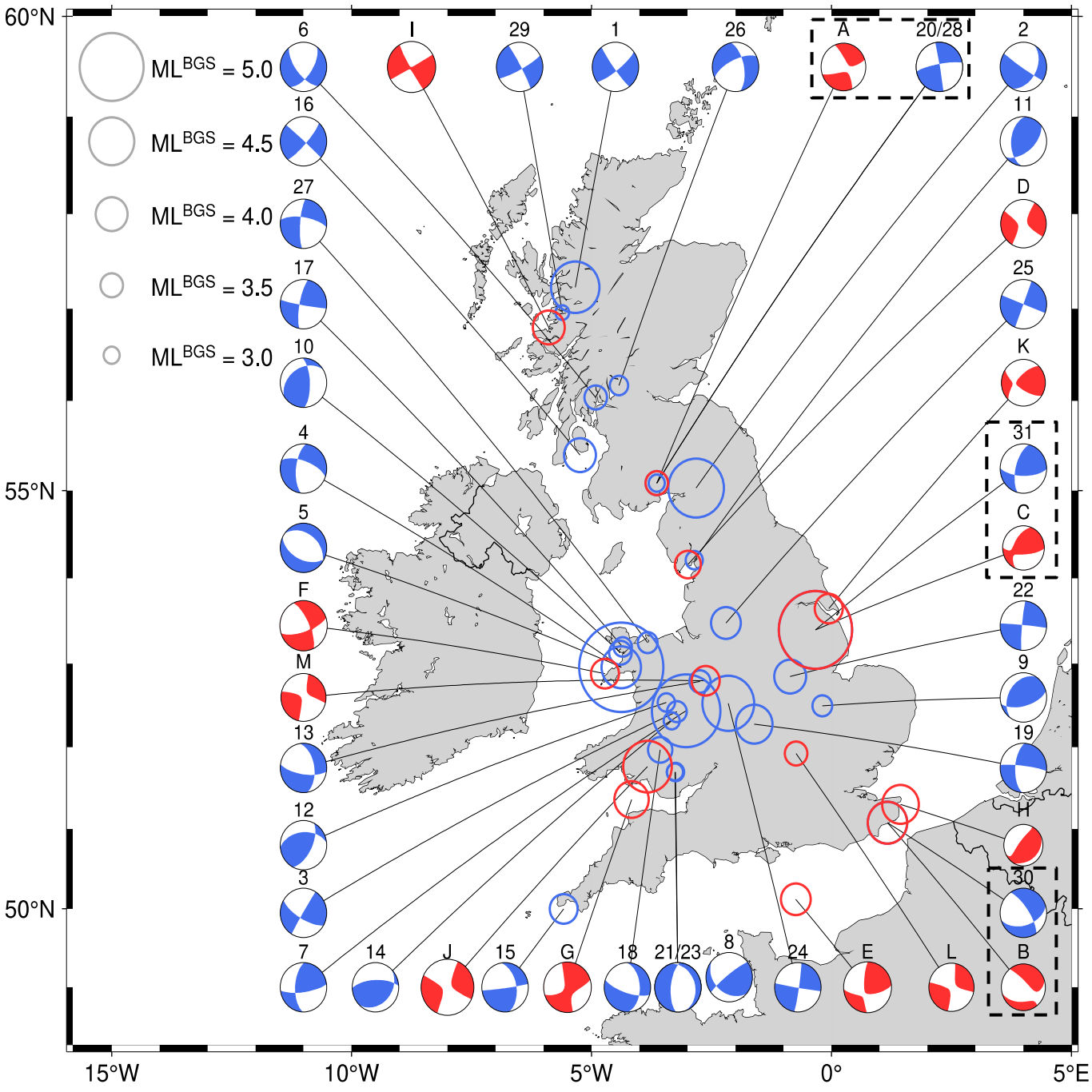

Figure 8 Moment tensors estimated for UK earthquakes from this study (red) and Baptie (2010; blue). Numbers correspond to events in Table 1 of Baptie (2010), and letters correspond to events in table 1 (this study), with events in common highlighted with a dashed box. Circle size for each event is scaled by ML^{BGS} value.

For shear faulting, the DC component should comprise most of the focal mechanism (e.g., Vavryčuk, 2015). Therefore, the large DC component in our preferred solution is a good indication of a reliable moment tensor solution.

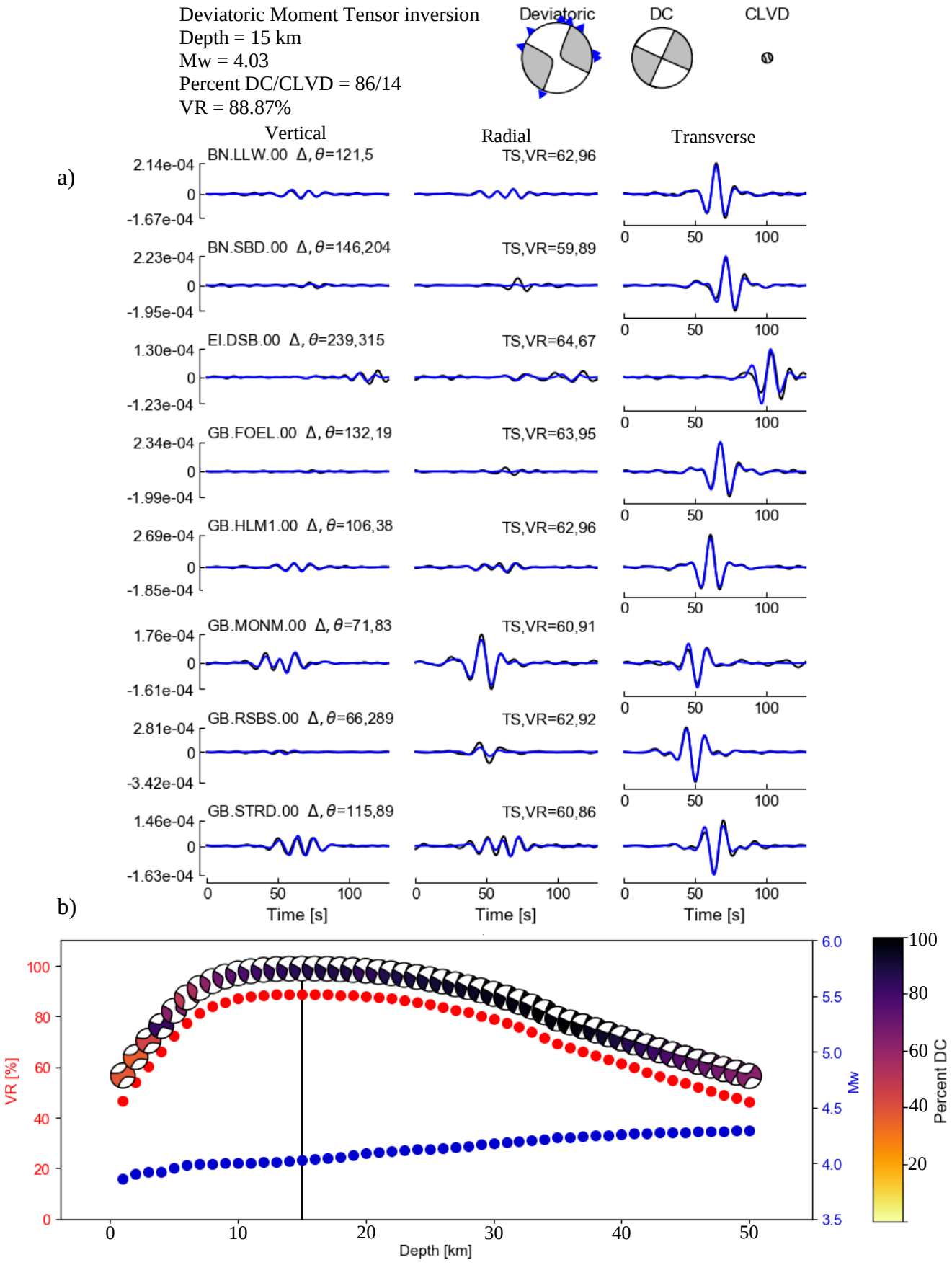

Figure 9 Moment tensor inversion results for event J calculated using MTtime. (a) Summary of the best-fitting inversion results and waveform fits at each station. Blue triangles on the lower hemisphere stereographic projection show station azimuth. From left to right, the values provided for each station are Δ (distance in km), θ (azimuth), time shift in samples (TS), and variance reduction (VR). (b) Moment tensor solution and M_W as a function of source depth. The colour of the moment tensor reflects the percentage DC (double couple) component of each solution. The vertical black line indicates the best-fitting solution.

The azimuthal station coverage for each event influences the stability of the moment tensor solution, and the non-DC component of the moment tensor solution. This is demonstrated by Petersen *et al.* (2021), who calculate moment tensors for three earthquakes occurring in The Alps, central Europe (M_W 3.5, 3.9 and 4.1) recorded by the dense AlpArray Seismic Network. This network provides excellent azimuthal coverage for moderate to large earthquakes in the region. Petersen *et al.* (2021) take advantage of the large number of stations in this network to investigate the stability of the moment tensor inversion to gaps in the azimuthal station distribution. They observe a clear increasing non-DC component trend with decreasing azimuthal coverage for the M_W 3.9 event; with a 180° station azimuthal coverage the non-DC component is only 10%, but this increases to 40 % when the station azimuthal coverage is only 45°. The moment tensor calculated for the Cwmllynfell, South Wales earthquake (Figure 8) had an azimuthal coverage of 270°. This azimuthal coverage is typical for the other events in our dataset, excluding a few events in northern England and Scotland, which only have azimuthal coverages of 180°. By only selecting events that have good station azimuthal coverage (>180°) for each of our moment tensor calculations, ensures that the non-DC component should remain low (Petersen *et al.*, 2021).

We compare focal mechanisms estimated in this study to those found by Baptie (2010; Figure 8). Collectively, these mechanisms demonstrate a range of faulting regimes, even for closely separated earthquakes (e.g., events 5 and 17, separated by 25 km). For the three events in common between this study and Baptie (2010), the focal mechanisms are comparable (Baptie (2010) focal mechanisms are based on P-wave first motions and are therefore constrained to be pure DC solutions).

3.1.2 Spectral modelling results

We estimate stable M_W and apparent stress for 13 UK events (Table 2): spectra-derived M_W values range from 3.44 to 4.51, and apparent stress ranges from 0.55 MPa to 4.13 MPa. An example of our spectral modelling for an earthquake in Cwmllynfell, South Wales (event J) recorded at GB.KESW is shown in Figure 10. This station is 317 km from the earthquake source and the amplitude spectra is modelled between 0.2 - 30 Hz (where SNR > 3). The goodness of fit between the observed and synthetic spectra is quantified using the reduced chi-square statistic (χ^2_{red}), which suggests reasonable agreement for this station ($\chi^2_{\mathrm{red}} = 1.02$).

Any stations that demonstrate a poor fit (χ^2_{red} >> 1) or a narrow estimation bandwidth (< 10 Hz) are removed from the analysis to improve robustness. In total, data from a further nine stations are used for this event, to estimate an M_W of 3.98 and apparent stress of 2.07 MPa. We quantify M_W and apparent stress uncertainties by calculating the standard deviation of the population of single station estimates. For this event, the standard deviations of M_W and apparent stress are 0.13 and 0.98 MPa, respectively.

Despite few published apparent stress estimates for events in the UK, there are two events which we can compare to the results of this study. The 28th April 2007 Folkestone (event B) and the 27th February 2008 Market Rasen (event C) earthquakes, we calculate apparent stresses of 1.22 and 4.13 MPa with standard deviations of 0.85 and 0.74 MPa, respectively. For the same events, Ottemöller and Sargeant (2010) estimate apparent stresses (converting their stress drop values to apparent stress using equation 10) of 0.7 ± 0.8 MPa and 8.0 ± 3.2 MPa. Even though the two studies use different methods and datasets the apparent stress estimates for these two events are comparable.

3.1.3 Coda calibration results

Our calibration dataset includes 33 geographically separated UK events (Figure 6 and Table 3) with ML^{BGS} ranging between 2.9 and 5.2. Of these 33 events, eight are *validation events* and four are *reference events*. Event I was not used as a *validation* or *reference* event, due to a significant aftershock present in the waveform data that could influence the calibration. We limit the number of *reference events* to four to avoid path bias resulting from too many paths from a particular region (Holt *et al.*, 2021). The resultant M_W and apparent stress values of our calibration dataset range from 2.65 to 4.48 and 0.02 to 5.56 MPa. The remaining 21 events in the calibration dataset are *calibration* events used to improve the path terms.

Coda envelopes and moment rate spectra for *validation* event C, the 27th February 2008 Market Rasen earthquake, are shown in Figure 11. These envelopes exhibit low noise, and the synthetic envelopes compare well to the observed. The subsequent moment rate spectra agree with the validation spectra, and the difference in estimated M_W between the coda estimate and validation estimate is 0.04.

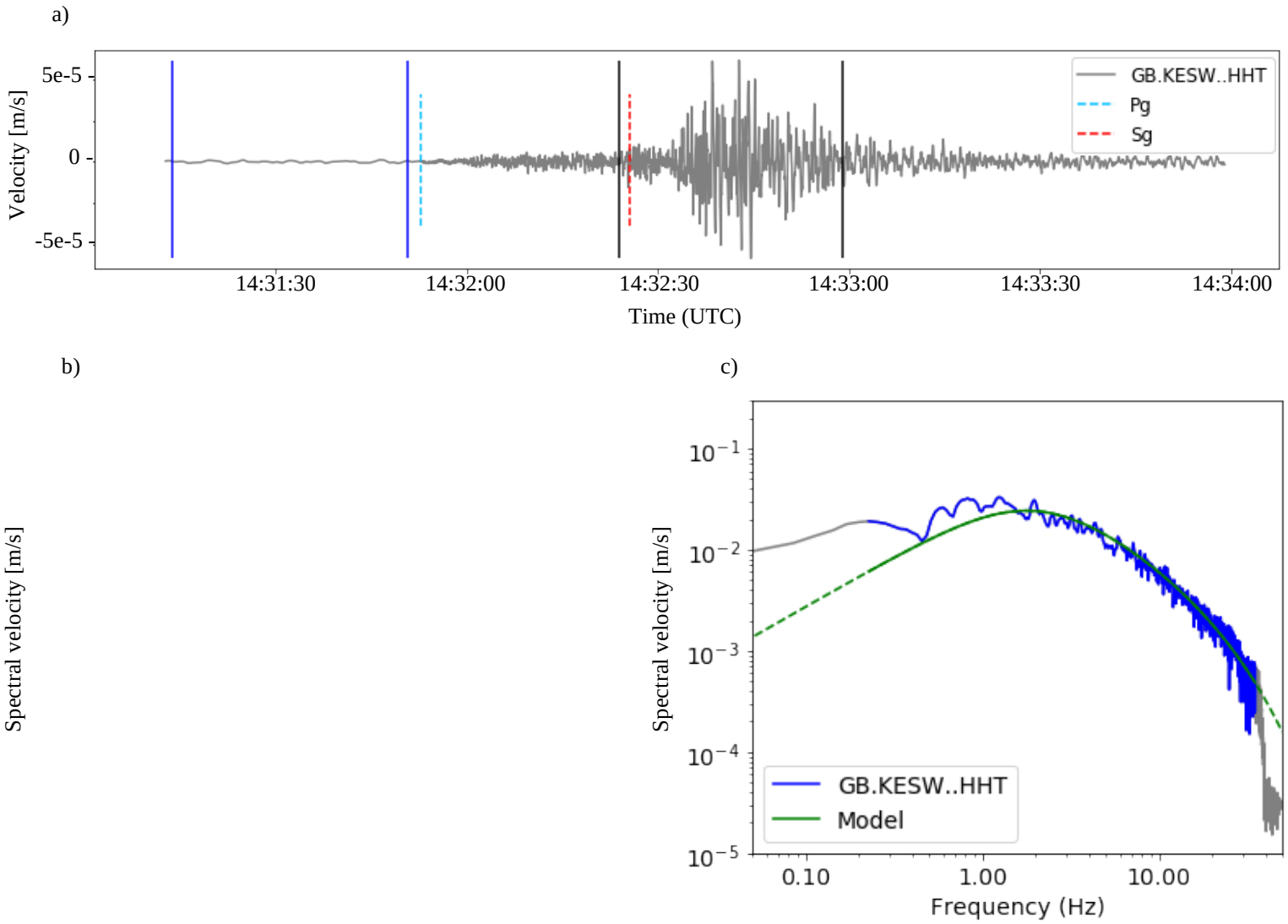

Figure 10 Spectral analysis of event J using SpecMod. (a) Broadband unfiltered, transverse component velocity recorded at GB.KESW showing manual Pg and Sg arrival picks and noise (blue) and signal (black) windows. The spectra of these windows are then shown in (b), where the dotted red lines represent the bandwidth (SNR ≥ 3) over which the signal is modelled. (c) Modelled signal spectrum. The signal spectrum is blue over the modelled bandwidth (0.2-30 Hz) and grey outside of this bandwidth. Likewise, the computed model (green) is solid within this bandwidth and dashed outside of it.

Event ID	f_c (Hz)	Ω_0 (m Ms)	Rupture radius (m)	M_0 (N-m)	M_w	Apparent stress (MPa)
A	2.29	0.41	317	1.73E+14	3.46 ± 0.09	0.55 ± 0.60
B	1.61	1.83	450	1.09E+15	4.00 ± 0.07	1.22 ± 0.85
C	1.34	8.98	541	6.44E+15	4.51 ± 0.10	4.13 ± 0.74
D	2.45	0.65	296	2.55E+14	3.57 ± 0.11	1.00 ± 0.49
E	2.33	0.98	312	4.04E+14	3.71 ± 0.14	1.36 ± 0.91
F	2.84	0.69	256	2.34E+14	3.55 ± 0.15	1.42 ± 0.58
G	2.96	0.68	245	2.20E+14	3.53 ± 0.08	1.52 ± 0.70
H	2.81	0.81	259	2.79E+14	3.60 ± 0.04	1.64 ± 0.51
I	2.16	0.96	336	4.29E+14	3.73 ± 0.05	1.15 ± 0.52
J	1.95	2.12	372	1.05E+15	3.98 ± 0.13	2.07 ± 0.98
K	3.07	0.51	237	1.59E+14	3.44 ± 0.07	1.22 ± 0.80
L	2.46	0.57	296	2.21E+14	3.53 ± 0.08	0.87 ± 0.54
M	3.02	0.57	241	1.82E+14	3.48 ± 0.10	1.33 ± 0.90

Table 2 Spectral analysis results from SpecMod. Note, uncertainties quoted for M_W and apparent stress are derived from the standard deviations of the single-station estimates.

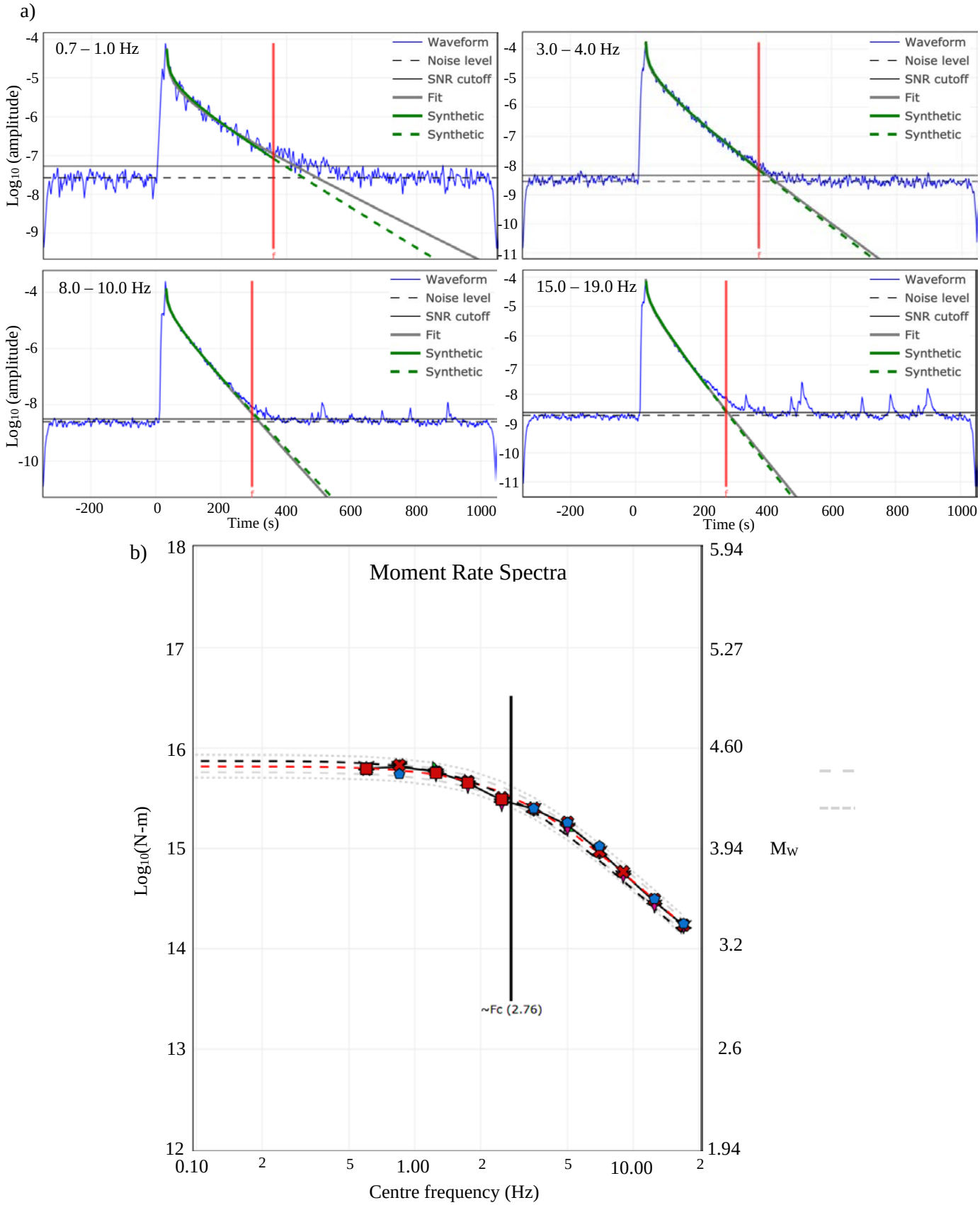

Figure 11 (a) Coda envelope fits for 4 narrowband frequencies at station GB.CWF. The f-marker/red bars represent the end of envelope fits, where the synthetics (green) transition from solid to dashed. (b) The resultant moment rate spectra used to calculate M_W for event C using the CCT. The symbols denote coda amplitudes at different stations, which are then averaged (black line) and modelled using the CCT to compute M_W (dashed red line). This model fit is compared to a reference, 'REF', (dashed black line), representing values of M_W and apparent stress from moment tensor inversion and spectral analysis, respectively. Confidence interval, UQ1 and UQ2, represent values that lie within the standard error and twice the standard error, respectively.

Origin time (Year-Month-Day Time)	Lat (°)	Lon (°)	ML^{BGS}	ML^{P}	M_W	Apparent stress (MPa)	Event type
2006-12-26 10:40:04	55.09	-3.64	3.5	3.5	3.40	0.38	C/V
2007-04-28 07:18:11	51.08	1.17	4.3	4.3	4.07	0.52	C/V
2008-02-27 00:56:47	53.40	-0.33	5.2	4.8	4.48	6.03	C/R
2008-05-28 20:09:08	54.69	-2.95	2.5	2.5	2.65	0.15	P
2008-09-30 20:46:32	58.08	-3.18	2.5	2.5	2.77	0.05	P
2008-10-10 04:28:39	56.83	-5.53	3.5	3.5	3.30	0.48	C
2008-10-26 18:06:25	52.20	-2.63	3.5	3.4	3.19	1.54	P
2008-11-03 09:53:42	56.37	-5.52	2.5	2.6	2.48	0.27	P
2009-03-03 14:35:55	51.12	1.18	3.0	3.1	2.99	0.32	P
2009-04-11 11:39:07	53.70	-0.25	3.0	2.9	2.88	1.00	P
2009-04-28 10:22:09	54.16	-2.99	3.7	3.7	3.48	0.36	C/R
2009-06-05 19:42:07	51.62	-3.65	2.9	2.9	2.74	0.30	P
2009-09-15 00:30:22	53.74	1.12	3.3	3.1	3.28	0.04	P
2009-09-30 13:04:56	53.70	-0.69	2.9	2.8	2.62	0.25	P
2009-10-06 05:05:55	51.77	-4.10	2.5	2.6	2.53	0.73	P
2010-07-30 23:39:39	51.67	-2.42	2.7	2.6	2.42	0.46	P
2010-11-13 09:37:00	53.22	-1.81	2.2	2.2	2.59	0.03	P/Q
2010-12-03 09:53:00	56.61	-5.53	2.2	2.1	2.40	0.20	P/Q
2010-12-04 01:53:25	53.98	0.87	2.6	2.7	2.68	0.02	P
2010-12-21 22:59:12	54.39	-3.15	3.5	3.5	3.28	0.96	C
2011-01-03 21:03:28	54.17	-1.65	3.6	3.1	3.07	0.57	C
2011-01-23 06:02:49	56.82	-5.78	3.5	3.4	3.28	0.79	C
2011-01-27 06:04:13	50.00	-1.91	2.5	2.4	2.51	0.24	P
2011-05-17 14:14:00	56.60	-5.60	2.2	2.3	2.79	0.03	P/Q
2011-06-23 13:43:38	50.57	-3.73	2.7	2.6	2.70	0.18	P
2011-07-14 06:59:10	50.12	-0.74	3.9	3.6	3.58	0.97	C/V
2011-08-21 08:37:23	56.85	-5.67	2.9	2.9	2.83	0.22	P
2011-09-08 19:02:51	56.59	-5.64	4.5	4.1	3.92	2.46	P
2012-01-18 18:33:29	49.63	-4.92	3.5	3.3	3.31	0.16	P
2012-02-20 05:35:48	55.78	-6.35	2.6	2.6	2.61	0.10	P
2012-02-26 22:31:16	54.65	-0.84	2.9	2.5	2.74	0.02	P
2012-02-29 09:14:26	55.78	-6.34	2.8	2.8	2.79	0.07	P
2012-03-04 23:23:53	56.24	-4.77	2.8	2.9	2.74	0.22	P
2012-06-01 12:16:46	52.41	-2.62	2.8	2.6	2.58	0.55	P
2012-10-31 15:59:19	55.97	-5.94	2.7	3.0	2.71	0.49	P
2012-12-14 23:03:03	50.96	-0.82	2.9	2.9	2.80	0.51	C
2013-01-18 05:20:44	52.80	-1.25	2.9	2.7	2.65	0.30	C
2013-02-27 23:57:01	52.90	-1.04	2.5	2.3	2.38	0.13	P
2013-05-15 17:43:48	57.67	-5.58	2.8	2.9	2.85	0.26	P
2013-05-18 19:18:02	56.78	-5.71	2.9	3.0	2.84	0.30	P
2013-05-29 03:16:28	52.88	-4.72	3.8	3.9	3.61	1.23	C/V
2013-06-26 22:28:01	52.88	-4.72	2.7	2.9	2.92	1.10	P
2013-06-26 22:28:29	52.88	-4.70	2.5	2.9	2.74	0.26	P
2013-07-16 04:04:00	57.72	-5.72	2.8	2.8	2.69	0.45	P
2013-08-25 05:37:48	53.86	-3.38	2.5	2.5	2.71	0.07	P
2013-08-25 09:58:36	53.88	-3.40	3.3	3.3	3.34	0.09	C
2013-08-27 10:06:06	56.64	-4.37	2.8	2.8	2.53	0.39	P
2013-08-31 06:36:11	53.89	-3.40	2.6	2.7	2.77	0.08	P
2014-02-20 13:21:30	51.36	-4.16	4.1	3.7	3.63	0.67	C/V
2014-04-17 06:07:14	52.72	-0.73	3.2	3.0	2.88	0.64	C
2014-04-18 06:50:51	52.72	-0.73	3.5	3.4	3.22	0.35	C

2014-06-18 08:44:39	53.40	-1.38	2.8	2.7	2.62	0.57	P
2014-06-20 16:01:48	55.79	-6.38	2.5	2.6	2.52	0.28	P
2014-07-03 18:36:08	56.82	-5.26	2.9	3.0	2.90	0.39	P
2014-07-11 11:54:32	49.15	-2.41	4.3	3.9	3.85	0.99	P
2014-07-23 16:26:41	49.10	-2.40	3.3	3.1	3.08	0.50	P
2014-07-25 19:05:25	53.72	1.39	2.7	2.6	2.69	0.04	P
2014-10-28 19:16:54	53.06	-1.19	2.6	2.7	2.82	0.06	P
2014-11-14 11:23:58	55.10	-3.65	2.6	2.9	2.66	0.41	P
2015-01-27 18:30:17	51.07	-1.30	2.9	2.8	2.96	0.03	C
2015-01-28 22:25:53	52.73	-0.72	3.8	3.6	2.78	0.55	C
2015-02-25 22:55:07	49.09	-2.38	3.0	2.9	2.90	0.45	P
2015-05-22 01:52:17	51.30	1.44	4.2	4.1	3.71	1.81	C/R
2015-05-26 15:41:03	53.12	-4.36	3.0	3.0	2.78	0.55	C
2015-05-30 19:20:12	54.33	-1.86	2.6	2.3	2.29	0.28	P
2015-09-22 21:40:11	52.70	-0.72	2.8	2.6	2.57	0.41	P
2017-03-03 09:28:11	52.91	-2.15	2.6	2.6	2.51	0.38	P
2017-08-04 14:45:34	56.80	-5.87	3.4	3.5	3.28	0.93	C
2017-11-01 20:59:22	55.88	-5.43	2.6	2.8	2.75	0.20	P
2018-02-17 14:31:07	51.77	-3.83	4.6	4.6	4.04	2.68	C/R
2018-02-28 07:33:51	54.64	-3.34	3.4	3.2	3.02	0.35	C
2018-03-09 08:14:08	52.76	-3.60	2.7	2.7	2.61	0.57	P
2018-04-01 11:10:58	51.16	-0.26	2.6	2.6	3.12	0.01	P/N
2018-04-29 18:19:00	55.89	-5.58	2.6	2.7	2.68	0.10	P
2018-05-01 06:15:59	55.89	-5.58	2.5	2.7	2.57	0.29	P
2018-06-09 22:14:28	53.65	-0.05	3.8	3.7	3.41	0.70	C/V
2018-06-27 12:28:24	51.18	-0.24	2.6	2.6	3.10	0.01	P
2018-07-05 10:53:24	51.15	-0.27	3.0	3.0	3.36	0.02	P/N
2018-08-02 17:42:52	52.61	0.45	2.7	2.5	2.46	0.84	P
2018-08-28 04:59:21	54.42	-0.88	2.8	2.4	2.35	0.73	P
2018-09-15 18:39:09	54.57	-1.64	3.1	2.8	2.70	0.38	C
2019-02-27 03:42:21	51.16	-0.25	3.1	3.2	3.45	0.02	C
2019-04-08 01:49:27	52.84	-2.60	2.5	2.6	2.61	0.19	P
2019-08-26 07:30:47	53.79	-2.96	2.9	2.6	2.79	0.04	C/H
2019-12-05 22:49:18	51.12	-2.98	3.2	3.2	2.90	0.38	C
2020-01-23 05:57:00	54.59	-1.31	3.1	2.9	2.79	0.23	C
2020-08-21 17:41:52	57.18	-5.77	2.6	2.6	2.59	0.41	P
2020-09-08 08:45:28	51.93	-0.74	3.5	3.6	3.50	0.16	C/V
2020-09-22 08:32:15	51.92	-0.68	3.0	3.0	3.01	0.15	C
2020-10-04 18:43:42	56.27	-3.75	2.5	2.7	2.74	0.07	P
2020-10-21 02:49:34	53.35	-0.57	2.5	2.3	2.23	0.41	P
2021-05-15 15:02:47	58.55	-4.72	2.5	2.6	2.66	0.20	P
2021-05-16 15:16:49	51.60	-2.80	2.9	3.0	2.82	0.31	P
2021-07-26 10:01:21	55.81	-3.20	2.5	2.6	2.55	0.50	P
2021-11-16 01:44:07	56.03	-5.54	3.4	3.4	3.15	0.24	C
2021-12-11 17:32:58	57.85	-5.11	2.5	2.5	2.49	0.27	P
2021-12-11 17:37:53	57.85	-5.11	2.5	2.5	2.52	0.24	P
2022-02-21 22:59:29	52.54	-1.94	2.8	2.8	2.61	0.60	P
2022-05-30 14:36:57	52.80	-2.62	3.8	3.7	3.40	1.47	C/V
2022-06-01 01:51:22	53.80	-2.24	2.7	2.7	2.54	0.30	P

Table 3 All events processed using the CCT (Coda Calibration Tool). Event origin time, latitude, and longitude from BGS earthquake bulletin. Event type includes Validation (V), Reference (R), Calibration (C), CCT processed (P), Quarry (Q), Newdigate (N), and hydrofrac (H)

Once the CCT calibration is finalised, we use the resultant calibration parameters (i.e., $W(f_b)$, $S(f_b)$, and $P(f_b, x)$ in Equation 11) to calculate M_W and apparent stress for an additional 64 UK events with $ML^{BGS} \geq 2.5$. These coda-derived M_W and apparent stress estimates range from 2.23 to 3.92 and 0.01 to 2.46 MPa. Considering a similar magnitude range for UK seismicity, our CCT-derived apparent stress estimates are comparable to those reported by Edwards *et al.* (2008). In addition, we analyse three ML^{BGS} 2.2 quarry events located in NW Scotland and in central England (Figure 6). CCT determines M_W values of 2.40, 2.59, and 2.79, and apparent stresses of 0.03, 0.03, and 0.20 MPa (Table 3) for these events. However, signals for these events have low SNRs at frequencies less than 2 Hz and are only observed at limited, close by seismic stations, therefore hindering the ability to model the spectra.

The CCT quantifies uncertainty by calculating confidence intervals for both M_W and apparent stress estimates based on the misfit of the inversion. The confidence interval limits are labelled UQ1 and UQ2, representing values that lie within the standard error and twice the standard error, respectively. In Figure 11, UQ1 and UQ2 follow the model fit closely, suggesting the uncertainty for this event is low. When compared to model fits in the calibration dataset, the mean M_W UQ2 lower and upper values are [-0.05, +0.05] and the mean apparent stress UQ2 limits are [-0.17, +0.25] MPa.

CHAPTER 4: Discussion

For a subset of 12 events (Sections 3.1.2 to 3.2.2) we have determined M_W using three independent methods: moment tensor inversion, spectral analysis, and coda calibration, allowing us to compare the results of each method. Additionally, this study is the first to analyse seismic coda for UK seismicity, providing a unique opportunity to compare coda observed for UK seismicity with coda observed in different tectonic settings.

4.1 Magnitude comparisons

Moment tensor estimated M_W compares well to spectral analysis estimated M_W (Figure 12). The mean difference between calculated M_W is 0.06, with a maximum difference of 0.10. The good agreement between M_W estimates using two independent methods suggests they are reliable. Additionally, we compare our coda calibration M_W estimates to those determined from moment tensor inversion (Figure 12b). These M_W estimates are also in good agreement,

with a mean difference of 0.03 and maximum of 0.07, indicating that the CCT has been effective in calibrating moment magnitudes across the UK.

We investigate the relationship between M_W with two local magnitude scales: ML^{BGS} (a local magnitude scale based on S-wave amplitudes) and ML^P (a local magnitude scale based on P-wave amplitudes). Using M_W estimates from spectral modelling (Sargeant and Ottemöller, 2009 and Ottemöller and Sargeant, 2010) Green *et al.* (2020) quantified the relationship between M_W with both ML^{BGS} and ML^P for UK events. Here we examine whether CCT M_W estimates produce similar relationships with ML^{BGS} and ML^P to those reported by Green *et al.* (2020). Calculating M_W using spectral modelling is reliant on several parameter choices (e.g., V_s, k, ρ, and θ in equations 6 and 7). The previously reported M_W estimates for the UK (Sargeant and Ottemöller, 2009 and Ottemöller and Sargeant, 2010) use different values for these parameters to those used in this study. Therefore, for consistency between the two M_W datasets, these previously reported M_W estimates (Sargeant and Ottemöller, 2009 and Ottemöller and Sargeant, 2010) are recalculated using the same parameter values as defined in this study and termed $M_{W,S\&O}$. Using orthogonal distance regressions, where the quoted uncertainties are $\pm$ 1 standard error, the relationships between $M_{W,S\&O}$ with ML^{BGS} and ML^P are:

$$M_{W,S\&O} = (0.71 \pm 0.05)\, ML^{BGS} + (0.77 \pm 0.16), \qquad 2.7 \leq ML^{BGS} \leq 5.2\,, \qquad [12]$$

$$M_{W,S\&O} = (0.91 \pm 0.05)\, ML^{P} + (0.21 \pm 0.15), \qquad 2.4 \leq ML^{P} \leq 4.8\,, \qquad [13]$$

ML^P is estimated for all events in the CCT dataset using the methodology of Green *et al.* (2020); the half peak-to-trough displacement values of the P-wave packet are measured, corrected for both propagation path and site effects, and resultant station magnitudes averaged across the recording network. The relationship between CCT M_W with ML^{BGS} and ML^P is calculated using the same regressions as before:

$$M_W = (0.73 \pm 0.03)\, ML^{BGS} + (0.71 \pm 0.11), \qquad 2.2 \leq ML^{BGS} \leq 5.2\,, \qquad [14]$$

$$M_W = (0.82 \pm 0.03)\, ML^{P} + (0.49 \pm 0.10), \qquad 2.1 \leq ML^{P} \leq 4.8\,, \qquad [15]$$

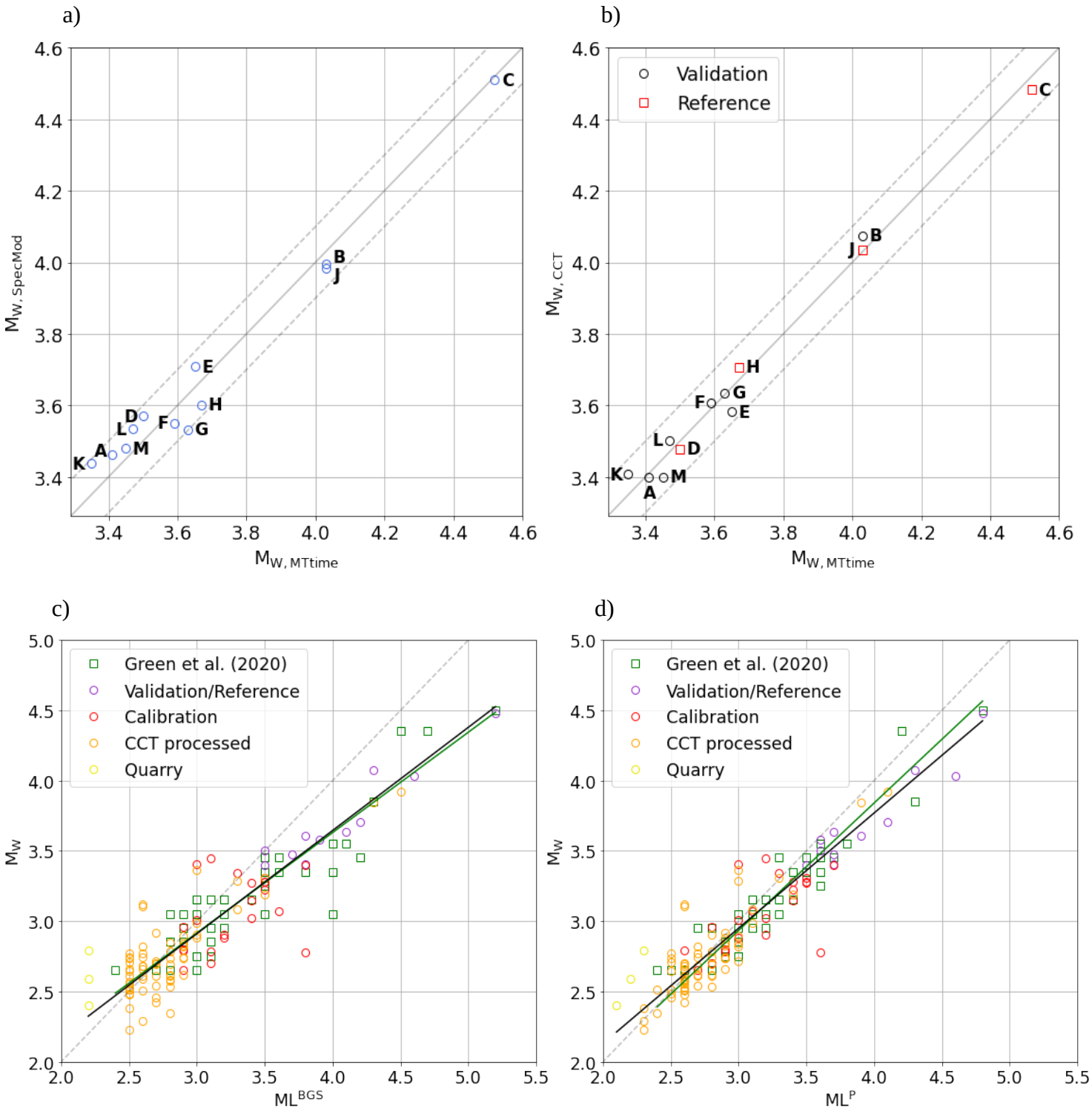

Figure 12 Comparison of magnitude estimates. Moment tensor inversion (MTtime) M_W estimates versus M_W estimates from spectral analysis (SpecMod); a) and CCT (b). In both (a) and (b), dotted lines represent values ±0.1 magnitude units from the 1:1 line. Data labels correspond to event IDs in Table 2. M_W estimates calculated using CCT versus ML^{BGS} (c) and ML^P (d). Linear regressions for our data and the data in Green et al. (2020) are computed using the Orthogonal Distance Regression method and shown in black and green, respectively.

Comparisons of Equation 12 with Equation 14, and Equation 13 with Equation 15 indicate that our results, using updated $M_{W,S\&O}$ values and a significantly expanded dataset (from 46 events to 100 events), are comparable with those of Green *et al.* (2020) (Figures 12c and 12d). However, our observations indicate that the gradient of the M_W: ML^P relationship is not consistent with a direct scaling between ML^P and M_W (i.e., the gradient is not 1). Therefore, this does not support the tentative hypothesis of Green *et al.* (2020) that ML^P scales with M_W due to the P-wave magnitude scale being less influenced than ML^{BGS} by estimation errors in along-path attenuation. In addition, by extending our results to lower magnitudes than Green *et al.* (2020) we observe more clearly that ML^{BGS} estimates are greater than M_W estimates at low magnitude, as is expected due to anelastic attenuation modifying the recorded spectra for smaller earthquakes (Deichmann *et al.*, 2017; Dost *et al.*, 2018).

4.2 Scaling of apparent stress and M_W

We analyse the relationship between our CCT estimates of moment magnitude and apparent stress (Figure 13). The CCT apparent stress is calculated by integrating the squared velocity spectrum, where the frequency range is extrapolated to zero and infinity at either end. In Figure 13, we include only events for which the extrapolated region is less than 45%, meaning at least 55% of the energy is observed. In all cases, this ensures the corner frequency is within the observed frequency range. Additionally, we categorise the UK events by location and origin time, allowing us to isolate the natural earthquakes from those related to anthropogenic sources (e.g., flow testing of an existing oil field). This allows us to focus only on sources where a Brune source model is applicable and thus provide more reliable apparent stress estimates. For comparison, we also include CCT results from Eastern Canada (Bent *et al.*, 2022) and Central Italy (Morasca *et al.*, 2022).

Figure 13 suggests two principal conclusions. Firstly, events with larger M_W result in larger values of apparent stress. This relationship is most apparent for the UK and Central Italy CCT results. However, this conclusion is tentative, since the trend of M_W with apparent stress has previously been explained by frequency limitations for lower magnitude events, where lower magnitude events are deficient in low frequencies and therefore appear to have lower apparent stress due to observational limitations. Secondly, the CCT apparent stress estimates from different tectonic regimes form distinct groups.

a)

b)

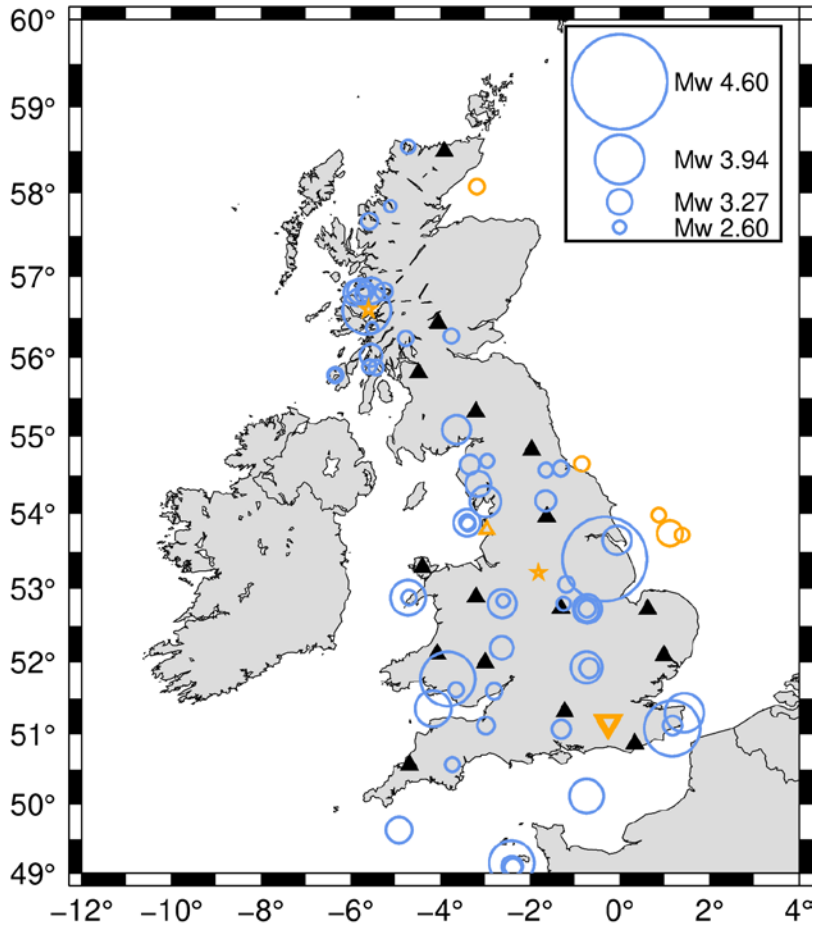

Figure 13 (a) Relationship between CCT moment magnitude and apparent stress estimates. Results include UK events analysed in this study (blue circles are onshore and English Channel earthquakes and orange symbols are North Sea or non-earthquake sources), events from Eastern Canada (black diamonds) and Central Italy (grey squares). (b) Map showing BGS locations for UK events, where symbol size is scaled by CCT M_W.

The apparent stress values from events in Eastern Canada are approximately an order of magnitude greater than events of comparable moment magnitude in Central Italy. The UK events lie between Eastern Canada and Central Italy and are generally closer to the Eastern Canada events.

4.3 Comparisons of coda in other tectonic regimes

We compare our coda envelopes to those from events in previously well-studied regions, including the Western US, Eastern Canada, and Italy (Figure 14). Each event is recorded by a broadband station approximately 100 km from a source of similar magnitude; events in the UK, Western US, and Italy are estimated as M_W ~4.5, whilst the Eastern Canada event has an M_W estimate of 4.97 (Table 4).

Region	Origin time (Year-Month-Day Time)	Lat (°)	Lon (°)	M_W	Station code	Station Lat (°)	Station Lon (°)	Event-station distance (km)
Eastern Canada	2002-04-20 10:50:48	44.53	-73.73	4.97	MNT	45.50	-73.62	108
Western US	2006-08-03 03:08:13	38.35	-122.57	4.50	JRSC	37.40	-122.24	110
UK	2008-02-27 00:56:47	53.40	-0.33	4.7	CWF	52.74	-1.31	98
Italy	2016-09-03 01:34:13	42.77	13.13	4.3	CAFI	43.33	11.97	113

Table 4 Event and station information for the coda shown in Figure 14. MW estimates and event information are from the Saint Louis University Moment Tensor Determinations and the Northern California Earthquake Data Center Catalog (Western US event only).

At low frequencies (0.05 - 0.10 Hz), the coda envelopes are similar between different regions, and the steepness of the coda decay is comparable for each example event. However, as frequency increases, the shape of the coda envelopes become increasingly distinct and appear to divide into two separate categories: (a) the UK and Eastern Canada, and (b) Italy and Western US, where the decay of coda envelopes at high frequencies (> 8 Hz) are much faster in Italy and Western US compared to the UK and Eastern Canada.

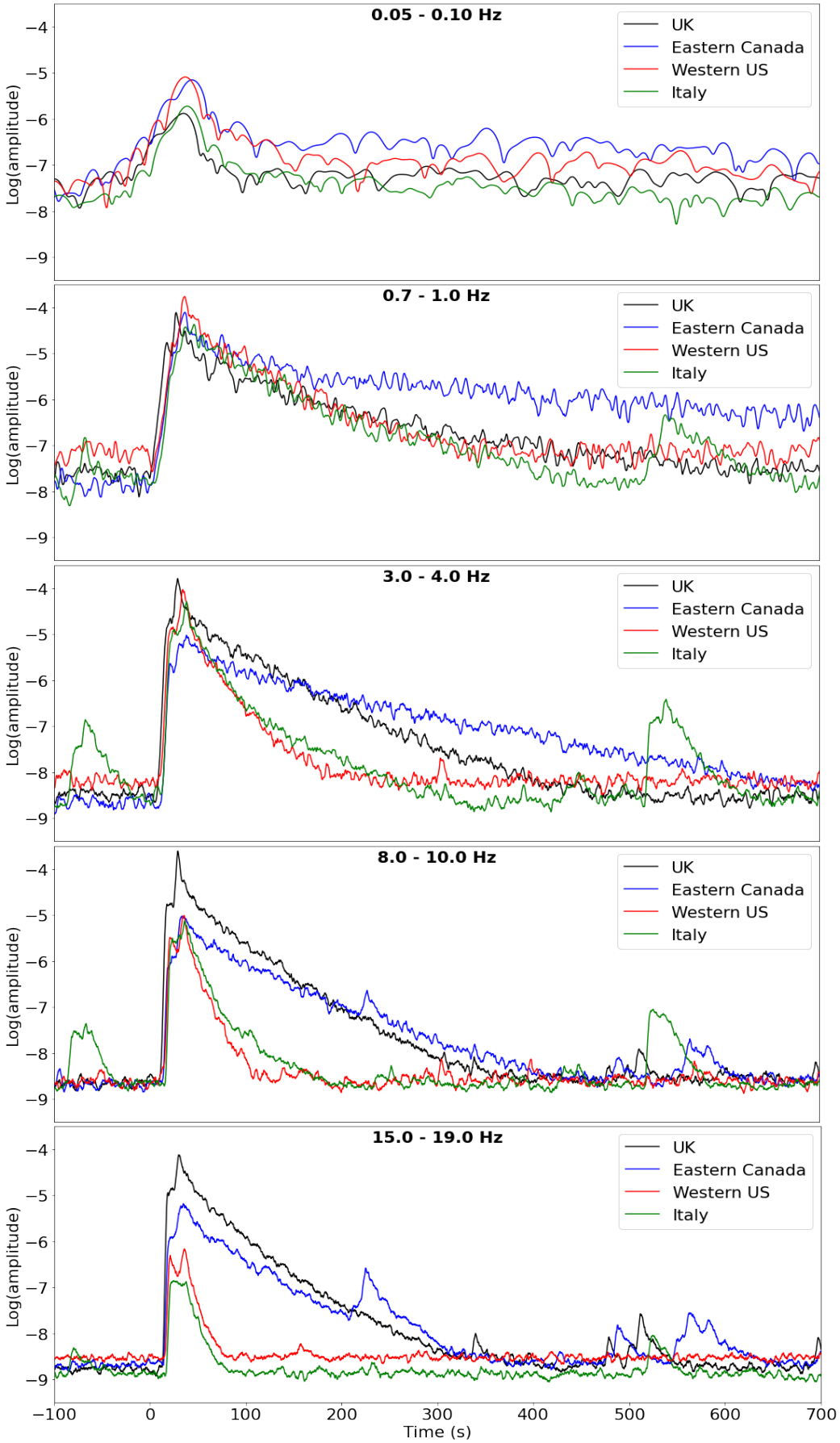

Figure 14 Coda envelopes from different regions for a range of frequencies. Representative events from different areas (see Table 4) are of comparable magnitude and recorded by broadband stations all approximately 100 km from each event.

The differences in envelope shape can be explained by regional variations in attenuation (e.g., Mayeda *et al.*, 1992). Coda Q describes the decay rate of narrowband local coda under the assumption of the single scattering model, first defined by Aki (1969) and subsequently used to characterise tectonic variation in a various regions (e.g., Havskov *et al*., 2016). Coda generation is due to 3-D scattering of seismic waves, which primarily results from subsurface impedance (Sato *et al.*, 2012). Variation in Q has been related to a variety of factors, including water content in the crust, heat flow, the degree of tectonic activity, and crustal age (e.g., Hauksson and Shearer, 2006). Italy and Western US are associated with high heat flow and frequent tectonic activity, resulting in low Q (e.g., Phillips *et al.*, 1988). In contrast, the UK and Eastern Canada have low heat flow and low levels of tectonic activity, resulting in high Q (e.g., Woodgold, 1990). The effect of these factors on coda decay increases with frequency, as seen in Figure 14, with differences in envelope shape being most apparent at 15 - 19 Hz. This is because lower frequency waves sample deeper parts of the lithosphere, which are more homogeneous than the shallowest parts of the lithosphere that are sampled by high frequency waves.

These regional differences in coda are consistent with previous local magnitude attenuation parameters calculated for the UK, which fall between the rapid amplitude reductions with range observed in Southern California and the slower amplitude decay observed in intra-plate areas such as Norway and the North-eastern US (Ottemöller and Sargeant, 2013). Low stress drop events are often located in areas of low Q, less competent rock, and higher heat flow (e.g., Zoback, 1991).

For example, Western US is a region of high heat flow. This is caused by active tectonic activity, marked by subduction zones, extensional tectonics, and volcanic activity. These geological factors create pathways for heat from the Earth's interior to reach the surface, leading to elevated geothermal gradients (e.g., Smith and Siegel, 2000). As a result, stress drop values range between 0.1 and 4.7 MPa for events of $M_W \leq 4.5$ (Mayeda *et al.*, 1996). In contrast, the UK is an area of high stress drop (and apparent stress), with values of stress drop ranging from 0.03 to 25.91 MPa for a similar magnitude range (e.g., Edwards *et al.*, 2008). These significant differences in coda decay between regions highlights that region-specific coda calibration is necessary; hence the derived calibration parameters in this study will be useful for future studies of seismic coda in the UK.

Conclusions

4.4 Overview of the thesis

M_W's have been calculated for 100 UK seismic events post 2006 (with $2.23 \leq Mw \leq 4.48$) using coda measurements. The data analysis, including the calibration of path and site effects were undertaken using the open-source software CCT (Barno, 2017) based upon the methodology of Mayeda *et al.* (2003).

Our analysis calibrates coda at 16 broadband UK seismic stations, which were chosen for their wide geographical coverage and long deployment history. To achieve the calibration of path and site effects we use 33 events distributed across the UK. To calibrate source size effects, M_W and apparent stress values for a subset of 12 events were independently estimated using moment tensor inversion and spectral modelling. We apply the calibrated magnitude estimation technique to a further 67 events. The CCT derived Mw values are within ± 0.1 magnitude units of these estimated for the eight *validation* events, providing confidence that the calibration is robust.

Our extended M_W catalogue for the UK allows us to compare the estimated M_W values with local magnitude scale estimates (ML^{BGS}, ML^{P}) at lower magnitudes than in previous studies (e.g., Green *et al.*, 2020). This study confirms that ML is greater than M_W for small magnitude UK earthquakes, which is expected from both theory and observations (e.g., Deichmann, 2017). UK earthquake coda decay rates are comparable to those in other intra-plate (e.g., Eastern Canada) regions rather than tectonically active regions (e.g., Western US, Italy).

The UK coda derived M_W catalogue has the advantage over previous studies that it has been generated using a common approach. The derived coda calibration parameters will allow rapid M_W estimation for future UK events to lower magnitude values (i.e., $M_W > 2.2$) than is currently feasible with moment tensor inversion techniques.

4.5 Future work

The reliability and robustness of this coda calibration technique could be enhanced with further work. For instance, future work could include increasing the density and coverage of source-to-receiver paths used within the coda calibration. It may be particularly beneficial to geographically extend the station network (for example by including stations in Eastern Ireland) to improve robustness when analysing events at the edges of the UK.

Additionally, the methods used to calculate the reference apparent stress values could have been more robust. In the spectrum analysis, site amplification factors are not considered, and a frequency-independent path effect is assumed (i.e., t*). The significance of these assumptions means that the reference apparent stress values may influence or bias the CCT-derived apparent stress values. A more thorough approach would have been to additionally consider these site amplification factors to more reliably and accurately derive the reference apparent stress values. However, the consequence of this assumption is diminished when considering M_W. Discounting site amplification is more relevant for the higher frequency terms of the calibration, meaning apparent stress values are more likely to be influenced than M_W, which is instead sensitive to the low frequency terms of the calibration.

References

Aki, K., 1966. Generation and Propagation of G Waves from the Niigata Earthquake of June 16, 1964.: Part 2. Estimation of earthquake moment, released energy, and stress-strain drop from the G wave spectrum, *Bulletin of the Earthquake Research Institute, University of Tokyo*, **44**(1), 73-88.

Aki, K., 1969. Analysis of the seismic coda of local earthquakes as scattered waves, *J. geophys. Res.*, **74**(2), 615-631.

Aki, K., & Chouet, B., 1975. Origin of coda waves: source, attenuation, and scattering effects, *J. geophys. Res.*, **80**(23), 3322-3342.

Arrowsmith, S. J., Kendall, M., White, N., VanDecar, J. C., & Booth, D. C., 2005. Seismic imaging of a hot upwelling beneath the British Isles, *Geology*, **33**(5), 345-348.

Baptie, B., 2010. Seismogenesis and state of stress in the UK, *Tectonophysics*, **482**(1-4), 150-159.

Barno, J., 2017. *LLNL/coda-calibration-tool*, Computer Software, https://github.com/LLNL/coda-calibration-tool, USDOE, doi:10.11578/dc.20180306.1

Bent, A. L., Mayeda, K., Roman-Nieves, J. I., Shelly, D., & Barno, J., 2022. Coda envelope moment magnitudes and the re-evaluation of magnitude conversion relations for seismic Hazard assessment in southeastern Canada, *Seismol. Res. Lett.*, **93**, 1325-1326.

Bluck, B. J., Gibbons, W., & Ingham, J. K., 1992. Terranes, *In Atlas of Palaeogeography and Lithofacies*, Cope, J. C., Ingham, J. K., Rawson, P. F., (Editors), Geological Society London, Memoirs, **13**, 1–4.

Boore, D. M., & Boatwright, J., 1984. Average body-wave radiation coefficients, *Bull. seism. Soc. Am.*, **74**(5), 1615-1621.

Bowers, D., and Selby, N. D., 2009. Forensic seismology and the comprehensive nuclear-test-ban treaty, *Annu. Rev. of Earth planet. Sci.*, **37**, 209-236.

Brune, J. N., 1970. Tectonic stress and the spectra of seismic shear waves from earthquakes, *J. geophys. Res.*, **75**(26), 4997-5009.

Chiang, A., & USDOE National Nuclear Security Administration, 2020. *Time Domain Moment Tensor Inversion in Python*. Computer software. *https://www.osti.gov//servlets/purl/1602708*. Vers. 0.1. USDOE National Nuclear Security Administration (NNSA).

Chiang, A., Dreger, D. S., Ford, S. R., Walter, W. R., & Yoo, S. H., 2016. Moment tensor analysis of very shallow sources, *Bull. seism. Soc. Am.*, **106**(6), 2436-2449.

Chiang, A., Gök, R., Tarabulsi, Y. M., El-Hadidy, S. Y., Raddadi, W. W., & Mousa, A. D., 2021. Seismic source characterization of the Arabian Peninsula and Zagros Mountains from regional moment tensor and coda envelopes, *Arab. J. Geosci.*, **14**, 9.

Deichmann, N., 2017. Theoretical basis for the observed break in ML/M w scaling between small and large earthquakes, *Bull. seism. Soc. Am.*, **107**(2), 505-520.

Dost, B., Edwards, B., & Bommer, J. J., 2018. The relationship between M and ML: a review and application to induced seismicity in the Groningen gas field, the Netherlands, *Seismol. Res. Lett.*, **89**(3), 1062-1074.

Dreger, D. S., 2003. TDMT_INV: Time domain seismic moment tensor inversion, In *International Geophysics*, Academic Press, **81**, 1627.

Dziewonski, A. M., & Anderson, D.L., 1981. Preliminary Reference Earth Model, *Phys. Earth Planet. Inter.*, **25**(297), 297-356.

Edwards, B., Allmann, B., Fäh, D., & Clinton, J., 2010. Automatic computation of moment magnitudes for small earthquakes and the scaling of local to moment magnitude, *Geophys. J. Int.*, **183**(1), 407-420.

El-Hadidy, S., Mohamed Adel, M.E., Deif, A., Abu El-Ata, S.A. and Moustafa Sayed, S.R., 2006. Estimation of frequency-dependent coda wave attenuation structure at the vicinity of Cairo Metropolitan area. *Acta Geodaetica Et Geophysica Hungarica*, *41*(2), pp.227-235.

Galloway, D., 2021. The British Geological Survey Earthquake Bulletin for 2020, *British Geological Survey Internal Report, OR/21/005.*

Gök, R., Barno, J., Mayeda, K., Roman-Nieves, J. I., & Walter, W. R., 2019, December. A New Coda Calibration Tool for Reliable Moment Magnitudes (Mw), *AGU Fall Meeting Abstracts*.

Green, D. N., Luckett, R., Baptie, B., & Bowers, D., 2020. A UK local seismic magnitude scale, MLP, using P-wave amplitudes, *Geophys. J. Int.*, **223**(3), 2054-2065.

Hanks, T. C., & Kanamori, H., 1979. A moment magnitude scale. *J. geophys. Res.*, **84**(B5), 2348-2350.

Hauksson, E., & Shearer, P.M., 2006. Attenuation models (Qp and Qs) in three dimensions of the southern California crust: Inferred fluid saturation at seismogenic depths, *J. geophys. Res.*, **111**, B05302.

Havskov, J., Sorensen, M. B., Vales, D., Ozyazicioglu, M., Sanchez, G., & Li, B., 2016. Coda Q in different tectonic areas, influence of processing parameters, *Bull. seism. Soc. Am.*, **106**(3), 956-970.

Herrmann, R. B., Benz, H., & Ammon, C. J., 2011. Monitoring the earthquake source process in North America, *Bull. seism. Soc. Am.*, **101**(6), 2609-2625.

Herrmann, R. B., 2013. Computer programs in seismology: An evolving tool for instruction and research, *Seismol. Res. Lett.*, **84**(6), 1081-1088.

Holt, J., Whidden, K. M., Koper, K. D., Pankow, K. L., Mayeda, K., Pechmann, J. C., Edwards, B., Gök, R., & Walter, W. R., 2021. Toward robust and routine determination of Mw for small earthquakes: Application to the 2020 Mw 5.7 Magna, Utah, seismic sequence, *Seismol. Res. Lett.*, **92**(2A), 725-740.

Kennett, B. L., Engdahl, E. R., & Buland, R., 1995. Constraints on seismic velocities in the Earth from traveltimes, *Geophys. J. Int.*, **122**(1), 108-124.

Laurendeau, A., Clément, C., & Scotti, O., 2022. A strategy to build a unified data set of moment magnitude estimates for low-to-moderate seismicity regions based on European–Mediterranean data: application to metropolitan France, *Geophys. J. Int.*, **230**(3), 1980-2002.

Madariaga, R., 1976. Dynamics of an expanding circular fault, *Bull. seism. Soc. Am.*, **66**(3), 639-666.

Main, I., Irving, D., Musson, R., & Reading, A., 1999. Constraints on the frequency—magnitude relation and maximum magnitudes in the UK from observed seismicity and glacio-isostatic recovery rates, *Geophys. J. Int.*, **137**(2), 535-550.

Malagnini, L., Bodin, P., Mayeda, K., & Akinci, A., 2006. Unbiased moment-rate spectra and absolute site effects in the Kachchh basin, India, from the analysis of the aftershocks of the 2001 M w 7.6 Bhuj earthquake, *Bull. seism. Soc. Am.*, **96**(2), 456-466.

Mayeda, K., Koyanagi, S., Hoshiba, M., Aki, K., & Zeng, Y., 1992. A comparative study of scattering, intrinsic, and coda Q− 1 for Hawaii, Long Valley, and central California between 1.5 and 15.0 Hz, *J. geophys. Res.*, **97**(B5), 6643-6659.

Mayeda, K., & Walter, W. R., 1996. Moment, energy, stress drop, and source spectra of western United States earthquakes from regional coda envelopes, *J. geophys. Res.*, **101**(B5), 11195-11208.

Mayeda, K., Hofstetter, A., O'Boyle, J. L., & Walter, W. R., 2003. Stable and transportable regional magnitudes based on coda-derived moment-rate spectra, *Bull. seism. Soc. Am.*, **93**(1), 224-239.

Mayeda, K., & Malagnini, L., 2010. Source radiation invariant property of local and near-regional shear-wave coda: Application to source scaling for the Mw 5.9 Wells, Nevada sequence, *Geophys. Res. Lett.*, **37**, L07306, doi:10.1029/2009GL042148.

Mayeda, K., Gök, R., Barno, J., Walter, W. R., & Roman-Nieves, J., 2020. The Coda Calibration and Processing Tool: Java-Based Freeware for the Geophysical Community. *EGU General Assembly 2020*, , Online, 4–8 May 2020, EGU2020-5874, https://doi.org/10.5194/egusphere-egu2020-5874.

Minson, S. E., & Dreger, D. S., 2008. Stable inversions for complete moment tensors, *Geophys. J. Int.*, **174**(2), 585-592.

Morasca, P., Mayeda, K., Gök, R., Phillips, W. S., & Malagnini, L., 2008. 2D coda and direct-wave attenuation tomography in northern Italy, *Bull. seism. Soc. Am.*, **98**(4), 1936-1946.

Morasca, P., Bindi, D., Mayeda, K., Roman-Nieves, J., Barno, J., Walter, W. R., & Spallarossa, D., 2022. Source scaling comparison and validation in Central Italy: data intensive direct S waves versus the sparse data coda envelope methodology, *Geophys. J. Int.*, **231**(3), 1573-1590.

Musson, R. M., 2007. British earthquakes, *Proceedings of the Geologists' Association*, **118**(4), 305-337.

Oth, A., Bindi, D., Parolai, S., & Di Giacomo, D., 2011. Spectral analysis of K-NET and KiK-net data in Japan, Part II: On attenuation characteristics, source spectra, and site response of borehole and surface stations, *Bull. seism. Soc. Am.*, **101**(2), 667-687.

Ottemöller, L., & Sargeant, S., 2010. Ground-motion difference between two moderate-size intraplate earthquakes in the United Kingdom, *Bull. seism. Soc. Am.*, **100**(4), 1823-1829.

Ottemöller, L., & Sargeant, S., 2013. A local magnitude scale ML for the United Kingdom, *Bull. seism. Soc. Am.*, **103**(5), 2884-2893.

Pasyanos, M. E., & Chiang, A., 2022. Full moment tensor solutions of US underground nuclear tests for event screening and yield estimation, *Bull. seism. Soc. Am.*, **112**(1), 538-552.

Petersen, G. M., Cesca, S., Heimann, S., Niemz, P., Dahm, T., Kühn, D., Kummerow, J., & Plenefisch, T., 2021. Regional centroid moment tensor inversion of small to moderate earthquakes in the Alps using the dense AlpArray seismic network: challenges and seismotectonic insights, *Solid Earth*, **12**(6), 1233-1257.

Phillips, W. S., Lee, W. H. K., & Newberry, J. T., 1988. Spatial variation of crustal coda Q in California, *PAGEOF*, **128**, 251-260.

Powell, M. J., 1964. An efficient method for finding the minimum of a function of several variables without calculating derivatives, *The Computer Journal*, **7**(2), 155-162.

Prieto, G. A., Parker, R. L., & Vernon III, F.L., 2009. A Fortran 90 library for multitaper spectrum analysis, *Computers & Geosciences*, **35**(8), 1701-1710.

Richter, C. F., 1935. An instrumental earthquake magnitude scale, *Bull. seism. Soc. Am.*, **25**(1), 1-32.

Sargeant, S., & Ottemöller, L., 2009. Lg wave attenuation in Britain, *Geophys. J. Int.*, **179**(3), 1593-1606.

Sato, H., Fehler, M. C., & Maeda, T., 2012. *Seismic wave propagation and scattering in the heterogeneous earth*, Springer Science & Business Media.

Shelly, D. R., Mayeda, K., Barno, J., Whidden, K. M., Moschetti, M. P., Llenos, A. L., Rubinstein, J. L., Yeck, W. L., Earle, P. S., Gök, R., Walter, W. R., 2022. A Big Problem for Small Earthquakes: Benchmarking Routine Magnitudes and Conversion Relationships with Coda Envelope-Derived M_w in Southern Kansas and Northern Oklahoma, *Bull. seism. Soc. Am.*, **112**(1), 210-225.

Singh, S. K., & Ordaz, M., 1994. Seismic energy release in Mexican subduction zone earthquakes, *Bull. seism. Soc. Am.*, **84**(5), 1533-1550.

Smith, R.B. and Siegel, L.J., 2000. *Windows into the Earth: the geologic story of Yellowstone and Grand Teton National Parks*. Oxford University Press.

Vavryčuk, V., 2015. Moment tensors: decomposition and visualization. In *Encyclopaedia of Earthquake Engineering*, Springer-Verlag, Berlin.

Wang, C. Y., & Herrmann, R. B., 1980. A numerical study of P-, SV-, and SH-wave generation in a plane layered medium, *Bull. seism. Soc. Am.*, **70**(4), 1015-1036.

Woodcock, N., & Strachan, R., 2012. *Geological History of Britain and Ireland*, Blackwell Publishing.

Woodgold, C. R., 1990. Estimation of Q in eastern Canada using coda waves, *Bull. seism. Soc. Am.*, **80**(2), 411-429.

Zoback, M. D., 1991. State of stress and crustal deformation along weak transform faults, *Philosophical Transactions of the Royal Society of London. Series A: Physical and Engineering Sciences*, **337**(1645), 141-150.